

The ANTARES Collaboration

Contributions to ICRC 2017

Part III: Searches for dark matter and exotics, neutrino oscillations and detector calibration

Contents

1 Neutrinos from Cosmic Ray Interactions in the Sun as background for dark matter searches	
PoS(ICRC2017) 907	5
2 Combined Search for Neutrinos from Dark Matter Annihilation in the Galactic Center using IceCube and ANTARES	
PoS(ICRC2017) 911	13
3 Indirect searches for dark matter with the ANTARES neutrino telescope	
PoS(ICRC2017) 913	20
4 Search for $\beta > 0.6$ magnetic monopoles with the ANTARES neutrino telescope	
PoS(ICRC2017) 953	28
5 Sensitivity of the ANTARES neutrino telescope to atmospheric neutrino oscillation parameters	
PoS(ICRC2017) 1026	36
6 Pointing accuracy of the ANTARES detector: Moon shadow and surface array analysis	
PoS(ICRC2017) 1053	44
7 Monitoring of the ANTARES optical module efficiencies using ^{40}K decays in sea water	
PoS(ICRC2017) 1058	51

*35th International Cosmic Ray Conference — ICRC2017
10–20 July, 2017, Bexco, Busan, Korea*

ANTARES Collaboration Author List

A. Albert¹, M. André², M. Anghinolfi³, G. Anton⁴, M. Ardid⁵, J.-J. Aubert⁶, T. Avgitas⁷,
B. Baret⁷, J. Barrios-Martí⁸, S. Basa⁹, B. Belhorma¹⁰, V. Bertin⁶, S. Biagi¹¹, R. Bormuth^{12,13},
S. Bourret⁷, M.C. Bouwhuis¹², H. Brânzaş¹⁴, R. Bruijn^{12,15}, J. Brunner⁶, J. Busto⁶,
A. Capone^{16,17}, L. Caramete¹⁴, J. Carr⁶, S. Celli^{16,17,18}, R. Cherkaoui El Moursli¹⁹, T. Chiarusi²⁰,
M. Circella²¹, J.A.B. Coelho⁷, A. Coleiro^{7,8}, R. Coniglione¹¹, H. Costantini⁶, P. Coyle⁶,
A. Creusot⁷, A. F. Díaz²², A. Deschamps²³, G. De Bonis¹⁶, C. Distefano¹¹, I. Di Palma^{16,17},
A. Domi^{3,24}, C. Donzaud^{7,25}, D. Dornic⁶, D. Drouhin¹, T. Eberl⁴, I. El Bojaddaini²⁶, N. El
Khayati¹⁹, D. Elsässer²⁷, A. Enzenhöfer⁶, A. Ettahiri¹⁹, F. Fassi¹⁹, I. Felis⁵, L.A. Fusco^{20,28},
P. Gay^{29,7}, V. Giordano³⁰, H. Glotin^{31,32}, T. Grégoire⁷, R. Gracia Ruiz^{7,33}, K. Graf⁴,
S. Hallmann⁴, H. van Haren³⁴, A.J. Heijboer¹², Y. Hello²³, J.J. Hernández-Rey⁸, J. Höfl⁴,
J. Hofestädt⁴, C. Hugon^{3,24}, G. Illuminati⁸, C.W. James⁴, M. de Jong^{12,13}, M. Jongen¹²,
M. Kadler²⁷, O. Kalekin⁴, U. Katz⁴, D. Kießling⁴, A. Kouchner^{7,32}, M. Kreter²⁷,
I. Kreykenbohm³⁵, V. Kulikovskiy^{6,36}, C. Lachaud⁷, R. Lahmann⁴, D. Lefèvre³⁷, E. Leonora^{30,38},
M. Lotze⁸, S. Loucatos^{39,7}, M. Marcelin⁹, A. Margiotto^{20,28}, A. Marinelli^{40,41},
J.A. Martínez-Mora⁵, R. Mele^{42,43}, K. Melis^{12,15}, T. Michael¹², P. Migliozzi⁴², A. Moussa²⁶,
S. Navas⁴⁴, E. Nezri⁹, M. Organokov³³, G.E. Pāvālaš¹⁴, C. Pellegrino^{20,28}, C. Perrina^{16,17},
P. Piattelli¹¹, V. Popa¹⁴, T. Pradier³³, L. Quinn⁶, C. Racca¹, G. Riccobene¹¹, A. Sánchez-Losa²¹,
M. Saldaña⁵, I. Salvadori⁶, D. F. E. Samtleben^{12,13}, M. Sanguineti^{3,24}, P. Sapienza¹¹,
F. Schüssler³⁹, C. Sieger⁴, M. Spurio^{20,28}, Th. Stolarczyk³⁹, M. Taiuti^{3,24}, Y. Tayalati¹⁹,
A. Trovato¹¹, D. Turpin⁶, C. Tönnes⁸, B. Vallage^{39,7}, V. Van Elewyck^{7,32}, F. Versari^{20,28},
D. Vivolo^{42,43}, A. Vizzoca^{16,17}, J. Wilms³⁵, J.D. Zornoza⁸, J. Zúñiga⁸.

¹GRPHE - Université de Haute Alsace - Institut universitaire de technologie de Colmar, 34 rue du Grillenbreit BP 50568 - 68008 Colmar, France

²Technical University of Catalonia, Laboratory of Applied Bioacoustics, Rambla Exposició, 08800 Vilanova i la Geltrú, Barcelona, Spain

³INFN - Sezione di Genova, Via Dodecaneso 33, 16146 Genova, Italy

⁴Friedrich-Alexander-Universität Erlangen-Nürnberg, Erlangen Centre for Astroparticle Physics, Erwin-Rommel-Str. 1, 91058 Erlangen, Germany

⁵Institut d'Investigació per a la Gestió Integrada de les Zones Costaneres (IGIC) - Universitat Politècnica de València. C/ Paranimf 1, 46730 Gandia, Spain

⁶Aix Marseille Univ, CNRS/IN2P3, CPPM, Marseille, France

⁷APC, Univ Paris Diderot, CNRS/IN2P3, CEA/Irfu, Obs de Paris, Sorbonne Paris Cité, France

⁸IFIC - Instituto de Física Corpuscular (CSIC - Universitat de València) c/ Catedrático José Beltrán, 2 E-46980 Paterna, Valencia, Spain

⁹LAM - Laboratoire d'Astrophysique de Marseille, Pôle de l'Étoile Site de Château-Gombert, rue Frédéric Joliot-Curie 38, 13388 Marseille Cedex 13, France

¹⁰National Center for Energy Sciences and Nuclear Techniques, B.P.1382, R. P.10001 Rabat, Morocco

¹¹INFN - Laboratori Nazionali del Sud (LNS), Via S. Sofia 62, 95123 Catania, Italy

- ¹²Nikhef, Science Park, Amsterdam, The Netherlands
- ¹³Huygens-Kamerlingh Onnes Laboratorium, Universiteit Leiden, The Netherlands
- ¹⁴Institute of Space Science, RO-077125 Bucharest, Măgurele, Romania
- ¹⁵Universiteit van Amsterdam, Instituut voor Hoge-Energie Fysica, Science Park 105, 1098 XG Amsterdam, The Netherlands
- ¹⁶INFN - Sezione di Roma, P.le Aldo Moro 2, 00185 Roma, Italy
- ¹⁷Dipartimento di Fisica dell'Università La Sapienza, P.le Aldo Moro 2, 00185 Roma, Italy
- ¹⁸Gran Sasso Science Institute, Viale Francesco Crispi 7, 00167 L'Aquila, Italy
- ¹⁹University Mohammed V in Rabat, Faculty of Sciences, 4 av. Ibn Battouta, B.P. 1014, R.P. 10000 Rabat, Morocco
- ²⁰INFN - Sezione di Bologna, Viale Berti-Pichat 6/2, 40127 Bologna, Italy
- ²¹INFN - Sezione di Bari, Via E. Orabona 4, 70126 Bari, Italy
- ²²Department of Computer Architecture and Technology/CITIC, University of Granada, 18071 Granada, Spain
- ²³Géozur, UCA, CNRS, IRD, Observatoire de la Côte d'Azur, Sophia Antipolis, France
- ²⁴Dipartimento di Fisica dell'Università, Via Dodecaneso 33, 16146 Genova, Italy
- ²⁵Université Paris-Sud, 91405 Orsay Cedex, France
- ²⁶University Mohammed I, Laboratory of Physics of Matter and Radiations, B.P.717, Oujda 6000, Morocco
- ²⁷Institut für Theoretische Physik und Astrophysik, Universität Würzburg, Emil-Fischer Str. 31, 97074 Würzburg, Germany
- ²⁸Dipartimento di Fisica e Astronomia dell'Università, Viale Berti Pichat 6/2, 40127 Bologna, Italy
- ²⁹Laboratoire de Physique Corpusculaire, Clermont Université, Université Blaise Pascal, CNRS/IN2P3, BP 10448, F-63000 Clermont-Ferrand, France
- ³⁰INFN - Sezione di Catania, Viale Andrea Doria 6, 95125 Catania, Italy
- ³¹LSIS, Aix Marseille Université CNRS ENSAM LSIS UMR 7296 13397 Marseille, France; Université de Toulon CNRS LSIS UMR 7296, 83957 La Garde, France
- ³²Institut Universitaire de France, 75005 Paris, France
- ³³Université de Strasbourg, CNRS, IPHC UMR 7178, F-67000 Strasbourg, France
- ³⁴Royal Netherlands Institute for Sea Research (NIOZ) and Utrecht University, Landsdiep 4, 1797 SZ 't Horntje (Texel), the Netherlands
- ³⁵Dr. Reimis-Sternwarte and ECAP, Friedrich-Alexander-Universität Erlangen-Nürnberg, Sternwartstr. 7, 96049 Bamberg, Germany
- ³⁶Moscow State University, Skobeltsyn Institute of Nuclear Physics, Leninskie gory, 119991 Moscow, Russia
- ³⁷Mediterranean Institute of Oceanography (MIO), Aix-Marseille University, 13288, Marseille, Cedex 9, France; Université du Sud Toulon-Var, CNRS-INSU/IRD UM 110, 83957, La Garde Cedex, France
- ³⁸Dipartimento di Fisica ed Astronomia dell'Università, Viale Andrea Doria 6, 95125 Catania, Italy
- ³⁹Direction des Sciences de la Matière - Institut de recherche sur les lois fondamentales de l'Univers - Service de Physique des Particules, CEA Saclay, 91191 Gif-sur-Yvette Cedex, France
- ⁴⁰INFN - Sezione di Pisa, Largo B. Pontecorvo 3, 56127 Pisa, Italy
- ⁴¹Dipartimento di Fisica dell'Università, Largo B. Pontecorvo 3, 56127 Pisa, Italy
- ⁴²INFN - Sezione di Napoli, Via Cintia 80126 Napoli, Italy
- ⁴³Dipartimento di Fisica dell'Università Federico II di Napoli, Via Cintia 80126, Napoli, Italy
- ⁴⁴Dpto. de Física Teórica y del Cosmos & C.A.F.P.E., University of Granada, 18071 Granada, Spain

Acknowledgements:

The authors acknowledge the financial support of the funding agencies: Centre National de la Recherche Scientifique (CNRS), Commissariat à l'énergie atomique et aux énergies alternatives (CEA), Commission Européenne (FEDER fund and Marie Curie Program), Institut Universitaire de France (IUF), IdEx program and UnivEarthS Labex program at Sorbonne Paris Cité (ANR-10-LABX-0023 and ANR-11-IDEX-0005-02), Labex OCEVU (ANR-11-LABX-0060) and the A*MIDEX project (ANR-11-IDEX-0001-02), Région Île-de-France (DIM-ACAV), Région Alsace (contrat CPER), Région Provence-Alpes-Côte d'Azur, Département du Var and Ville de La Seyne-sur-Mer, France; Bundesministerium für Bildung und Forschung (BMBF), Germany; Istituto Nazionale di Fisica Nucleare (INFN), Italy; Stichting voor Fundamenteel Onderzoek der Materie (FOM), Nederlandse organisatie voor Wetenschappelijk Onderzoek (NWO), the Netherlands; Council of the President of the Russian Federation for young scientists and leading scientific schools supporting grants, Russia; National Authority for Scientific Research (ANCS), Romania; Ministerio de Economía y Competitividad (MINECO): Plan Estatal de Investigación (refs. FPA2015-65150-C3-1-P, -2-P and -3-P, (MINECO/FEDER)), Severo Ochoa Centre of Excellence and MultiDark Consolider (MINECO), and Prometeo and Grisolia programs (Generalitat Valenciana), Spain; Ministry of Higher Education, Scientific Research and Professional Training, Morocco. We also acknowledge the technical support of Ifremer, AIM and Foselev Marine for the sea operations and the CC-IN2P3 for the computing facilities.

Neutrinos from Cosmic Ray Interactions in the Sun as background for dark matter searches

M. Ardid^a, I. Felis^a, M. Lotze^b and C. Tönnis^{b,1}, on behalf of the ANTARES Collaboration

^a*Institut d'Investigació per a la Gestió Integrada de les Zones Costaneres (IGIC) - Universitat Politècnica de València. C/ Paranimf 1, 46730 Gandia, Spain.*

^b*IFIC - Instituto de Física Corpuscular, CSIC - Universitat de València. C/ Catedrático José Beltrán 2, E-46980 Paterna, Valencia, Spain*

E-mail: mardid@fis.upv.es, ivfeen@upv.es, moritz.lotze@ific.uv.es, ctoennis@ific.uv.es

Neutrino telescopes have been proposed as efficient tools for indirect dark matter searches, especially using the Sun as source for its good capability to capture dark matter and since we do not expect high-energy neutrinos from it. However, the last statement should be taken with caution because high-energy neutrinos may come from cosmic particle interactions in the atmosphere of the Sun and producing neutrinos. In this work, we describe an analysis of the ANTARES neutrino telescope optimised for the observation of neutrinos coming from the atmosphere of the Sun due to cosmic particles interactions. Focusing in the 10 GeV - 10 TeV energy range and using 2007-2012 data, the sensitivity obtained for the flux is approximately $10^{12} \text{ km}^{-2} \text{ y}^{-1}$, whereas the expected flux is two order of magnitudes below. From this, we can conclude that present high-energy neutrino telescopes dark matter searches in the Sun can indeed neglect this contribution, but could play a role in future detectors with better neutrino flux sensitivities in the 10 GeV - 10 TeV energy range and very good angular resolution.

*35th International Cosmic Ray Conference – ICRC217-
10-20 July, 2017
Bexco, Busan, Korea*

¹Speaker

1. Introduction

There are several techniques to detect high energy neutrinos, but for the energy range of interest between 10^{10} and 10^{16} eV, the most exploited method is the detection with large volumes of dense material (such as water or ice) by photomultipliers sensitive to Cherenkov light. As neutrinos can interact with atomic nuclei to produce charged leptons that emit Cherenkov radiation in water, this optical pattern can be used to infer direction, energy, and more information about incident neutrinos. This is the technique used by the ANTARES underwater neutrino telescope [1]. Data from this detector have been used in different Dark Matter (DM) searches in the Sun [2] [3] [4]. In this kind of searches the neutrino flux produced by cosmic rays interacting with the atmosphere in the Sun is usually neglected. In this paper, we use the ANTARES detector to study this flux and to derive possible consequences for DM searches in the Sun through neutrino detection.

Cosmic ray impingement on the solar atmosphere leads to the production of secondary particles via high energy pp-interactions, the decay of which results in the flux of both electron and muon neutrinos and antineutrinos.

Studies of the flux of neutrinos originating from cosmic ray interactions with matter in the Sun have been performed with Monte Carlo models for high energy particle interactions [5] [6] [7] [8] [9]. To do this, it has been taken into account the interplanetary solar magnetic fields and the shadowing effect of inelastic neutrino scattering in the Sun. The Solar Atmosphere Neutrino (SA ν) spectra may be altered by neutrino oscillations, which depend on the neutrino mass differences and mixing matrices. The resulting flux at the Earth (within the Sun's solid angle) is higher than the corresponding one from cosmic ray interactions with the Earth atmosphere, so it is a potential source of background for dark matter searches based on detection of neutrinos coming from the Sun.

2. Expected neutrino fluxes from the Sun

In recent years, significant improvements have been made in the modelling of the solar atmosphere. Ingelman and Thunman [10] used a semi-empirical 1D model for solar density from the data of [11] for the atmosphere (updated in [12]) and [13] for the deeper layers of the Sun. It can be parameterized using the following expression: $\rho(h) = \rho_0 e^{-h/h_0}$, where $h > 0$ and $h < 0$ are the locations above and below the solar radius R_\odot , respectively. The parameters ρ_0 and h_0 are presented in Table 1.

h [km]	ρ_0 [g/cm ³]	h_0 [km]
$h > 0$	$3.68 \cdot 10^{-7}$	115
$-2000 < h < 0$	$3.68 \cdot 10^{-7}$	622
$h < -2000$	$45.3 \cdot 10^{-7}$	2835

Table 1. Parameters that define the profile of solar density.

The most current profiles [6] [7] start from this 1D model and complement it with additional requirements. In Figure 1 we show an outline of how the particles travel through the Sun, as well as the density profile. The incoming cosmic rays interact with the Sun creating secondary particles that interact or decay producing neutrinos. It is observed that, depending on

the angle of impact with respect to the axis connecting the Sun and Earth, the interaction length varies, being greater for smaller angles.

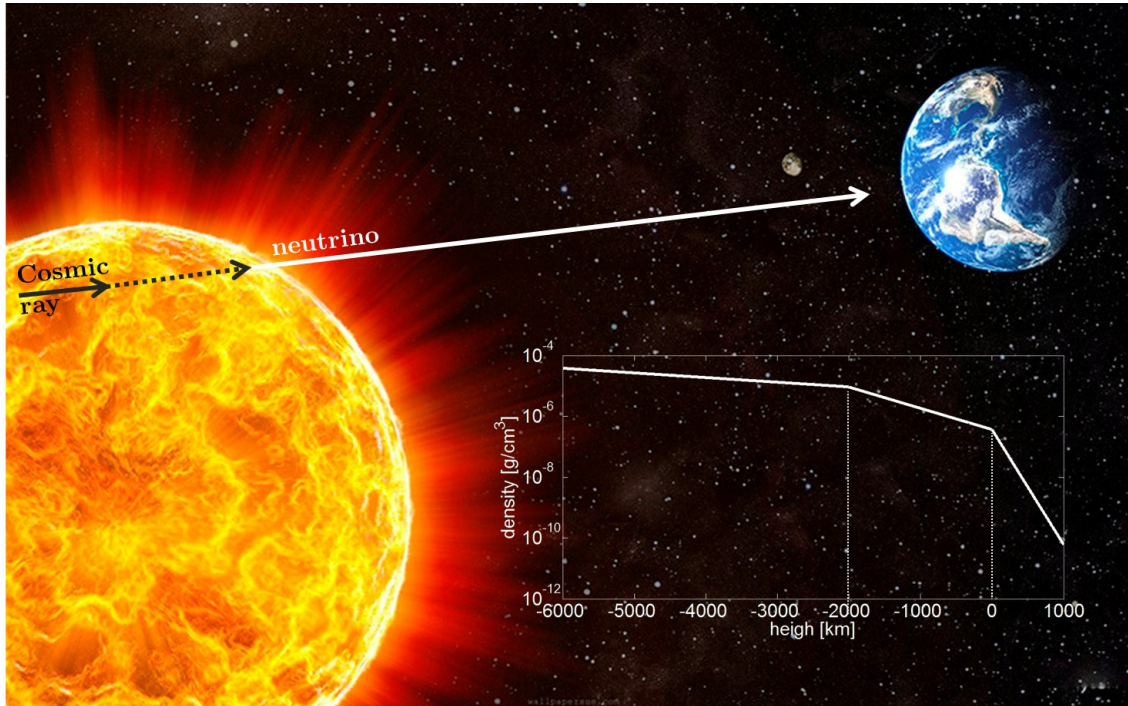


Figure 1. Neutrino production scheme of the solar atmosphere and density profile of the Sun.

In Figure 2 we show a first approximation of the expected SAV flux in the Earth without considering the oscillations (left) and considering the oscillations (right) [5]. For comparison, the flux of neutrinos from the Earth atmosphere is also shown on the left plot. We can infer that, for the energy range of interest (10 GeV - 10 TeV) the total expected flux is approximately $2.7 \cdot 10^{10} \text{ km}^{-2} \text{ y}^{-1}$.

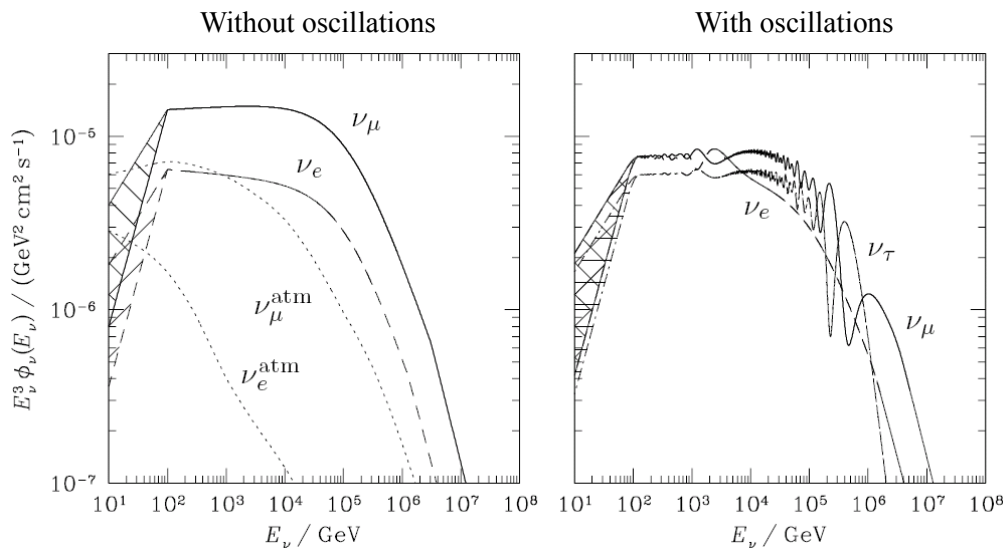


Figure 2. Comparison of expected atmospheric solar neutrino fluxes on Earth, with and without oscillation, for the three neutrino families. From [5].

From most recent studies [6] we extract the fluxes (Figure 3) from each of the neutrino and antineutrino flavours of the solar atmosphere that reach the Earth (solid line), compared to those produced in the solar atmosphere (discontinuous). Shaded bands show the region of uncertainty in all models. In this case, we have the dependence on the angle with respect to the solar centre. These fluxes have been used in the studies.

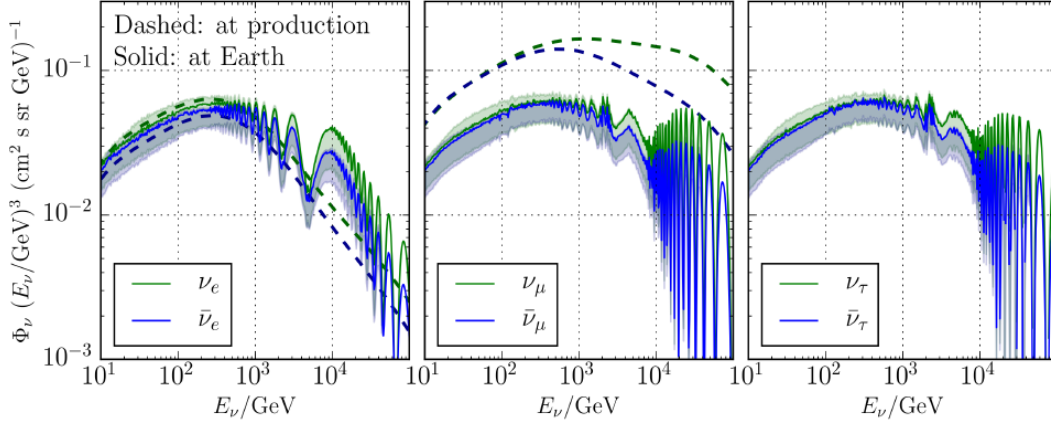


Figure 3. Fluxes of the three neutrino and antineutrino flavours at production in the atmosphere of the Sun and on Earth. From [6].

3. ANTARES search for neutrinos from cosmic ray interactions in the Sun

To place the most restrictive limits on a signal model, the strategy to choose the appropriate event selection is based on two steps:

1st Step. From a flux of particles known by a physical model of a source (e.g. the Sun) and the efficiency of the telescope (expressed through the effective area), we can obtain the sensitivity to that flux from a model of rejection. For this, the parametric cuts that optimize the sensitivity to this flux are looked for. Although we cannot know the actual upper limit that will result from an experiment until we see the data, we can use in this step the Monte Carlo predictions to calculate the sensitivity (average upper limit calculated according to Feldman-Cousins [14]) that would be observed after a hypothetical repetition of the experiments with an expected background, n_b , and no true signal ($n_s = 0$). This average upper limit, $\bar{\mu}_{90}$, is the sum of the expected upper limits, $\mu_{90}(n_{obs}, n_b)$, weighted by its probability of occurrence of Poisson, i.e.:

$$\bar{\mu}_{90}(n_b) = \sum_{n_{obs}}^{\infty} \mu_{90}(n_{obs}, n_b) \frac{(n_b)^{n_{obs}}}{(n_{obs})!} e^{-n_b} . \quad (1)$$

On a set of identical experiments, the strongest constraint on the expected flow of the signal Φ corresponds to the set of selection cuts that minimizes the model rejection factor and, therefore, minimizes the upper limit of average flow that would be obtained on the hypothetical experimental set. For the purposes of calculation with neutrino telescopes, we will use the following expression [15] [2]:

$$\bar{S}(n_b) = \Phi \frac{\bar{\mu}_{90}}{n_s} = \frac{\bar{\mu}_{90}}{A_{Eff} \cdot T} \quad (2)$$

where A_{Eff} is the average effective area in the energetic range in question for both neutrinos and antineutrinos and T is the live time of the detector.

2nd Step. With the values obtained in the first step, the flux observed by the telescope is searched applying these selection cuts and if no significant excess over background is observed the upper limit to the flux is established. Then, the corresponding upper limit at 90% confidence level of the flux from the source is [15]:

$$L(n_{obs}, n_b) = \Phi \frac{\mu_{90}(n_{obs}, n_b)}{n_s} = \frac{\mu_{90}(n_{obs}, n_b)}{A_{Eff} \cdot T} \quad (3)$$

As for the 2008-2012 analysis [3], a binned method is used in order to optimize the sensitivities of ANTARES in the search for neutrinos from cosmic ray interactions in the Sun. The Model Rejection Factor (MRF) is used to optimize the angular distance to the sources ($0 \leq \text{angle} \leq 3^\circ$) and the track quality cut parameter $0 \leq \chi^2 \leq 2$ for events detected with more than one line, so both zenith and azimuth of neutrino direction could be determined with good accuracy.

Table 2 summarises the results of the study. The selection parameters that optimise the sensitivity are shown. It is also presented the effective area times the live time of the detector for these parameters and the observed and expected background events. Finally, the SA_v flux sensitivity and upper limit obtained are shown.

Parameters		$A_{eff} \cdot T$	Events		Sensitivity	Upper flux Limit
χ^2	Angle [°]	[m ² ·d]	n_{obs}	n_b	[km ⁻² ·y ⁻¹] · 10 ¹²	[km ⁻² ·y ⁻¹] · 10 ¹²
1.4	2.1	$3.4 \cdot 10^{-4}$	1	1.8	3.9	3.5

Table 2. Values of the parameters that optimise the sensitivity, the effective area times the live time, the observed and expected background events, and the SA_v flux sensitivity and upper limit obtained.

4. Solar neutrino floors for ANTARES

We have derived the floor for Secluded Dark Mather (SDM) searches in the Sun with the ANTARES detector due to interactions of cosmic rays in the atmosphere of the Sun. Particularly, the case when two DM particles annihilates to meta-stable mediators which, in turn, decay into neutrino plus antineutrino [16] [4] [17] has been selected as example because of the enhanced signal in high-energy neutrino telescopes. For this purpose, we have to reinterpret the flux of SA_v in terms of flux for the SDM detection studies. A simplified approach to the problem is to weight the original neutrino flux ϕ_{AS_ν} with the effective areas for SDM and SA_v, as follows:

$$\phi_\nu = \phi_{AS_\nu} \cdot \frac{A_{Eff,AS_\nu}}{A_{Eff,SDM}}$$

From the optimization of the event selection criteria for SDM searches with ANTARES [4], we obtained the best sensitivities from neutrino fluxes using the Model Rejection Factor (MRF) method [15], as well as the effective areas $A_{Eff,SDM}$. With these best sensitivities we have the best quality and angular cuts. In addition, from the present study we obtain the corresponding effective areas $A_{Eff,AS\nu}$ for the resulting quality and angular cuts for SDM searches. We present the results of the floor for the case of mediator that decays directly into neutrinos, in which the neutrino signal is enhanced, and thus the one that first will reach the floor. This happens in the situation in which the mediator lifetime is long enough, so that the absorption of neutrinos in the Sun becomes negligible, but not so long that the mediator decays before reaching the Earth. In this scenario, for long-lived mediators ($L > 10^5$ km), the relationship between Γ and ϕ_ν is [4]:

$$\Gamma = \frac{4\pi D^2 \phi_\nu}{\frac{4}{3}(1 - e^{-D/L})}$$

where D is the distance between the Sun and the Earth and L is the mediator's decay length, $L = \gamma c \tau$, i.e. the product of the mediator's lifetime, τ , the speed of light, c , and the relativistic boost factor γ . The limits on the DM-proton cross sections have been derived assuming that there is equilibrium of the DM population in the Sun, and the same approximations shown in [4] [18]. Figure 4 shows the neutrino floor for SDM in the case of mediator decay into neutrino for a decay length of $2.8 \cdot 10^7$ km. Here, we only consider Spin-Dependent (SD) cross sections, as direct detection experiments are more efficient for testing the Spin-Independent cross sections. The floor for ANTARES is more than two orders of magnitude below the current limit. IceCube limit from [17] is closer to the neutrino floor, although this should be taken with caution since the floor does depend in the detector as well, and the floor presented here is for ANTARES.

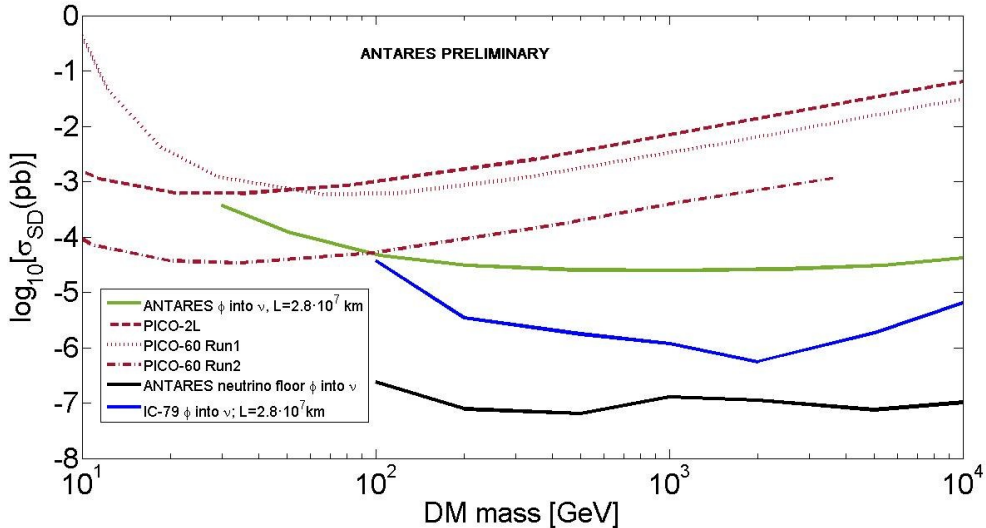


Figure 4. ANTARES neutrino floor due to $SA\nu$ for the SDM model in which the mediator decays directly into neutrinos. It is compared with the limits from ANTARES [4] and IceCube-79 [19] [17] and the limits from the direct detection experiments PICO [20] [21] [22] [23].

5. Conclusions

We have obtained the sensitivity of ANTARES for SAV flux, and derived an upper limit to this flux. We have also studied the SAV as a background to the signal from DM annihilation in the Sun. Particularly for SDM that annihilates into meta-stable mediators that decay into neutrinos. For this SDM case, in which we expect the largest flux, the floor due to SAV is still more than one order of magnitude below the current ANTARES upper limit. Anyway, the SAV flux will be an essentially irreducible background for neutrino searches from DM annihilation in the Sun, and thus, this background should be studied as well for the next generation of neutrino telescopes, such as KM3NeT [24].

Acknowledgements

We acknowledge the financial support of Plan Estatal de Investigación, ref. FPA2015-65150-C3-1-P and ref. FPA2015-65150-C3-2-P (MINECO/FEDER), Consolider MultiDark CSD2009-00064 (MINECO) and of the Generalitat Valenciana, Grant PrometeoII/2014/079.

References

- [1] M. Ageron et al., «ANTARES: The first undersea neutrino telescope,» *Nuclear Instruments and Methods in Physics Research A*, vol. 656, pp. 11-38, 2011.
- [2] S. Adrián-Martínez et al., «First results on dark matter annihilation in the Sun using the ANTARES neutrino telescope,» *Journal of Cosmology and Astroparticle Physics*, 2013.
- [3] S. Adrián-Martínez et al., «Limits on dark matter annihilation in the sun using the ANTARES neutrino telescope,» *Physics Letters B*, vol. 759, pp. 69-74, 2016.
- [4] S. Adrián-Martínez et al., «A search for Secluded Dark Matter in the Sun with the ANTARES neutrino telescope,» *Journal of Cosmology and Astroparticle Physics*, vol. 2016, n° 5, 2016.
- [5] C. Hettlage, K. Mannheim and J. Learned, «The Sun as a high-energy neutrino source,» *Astroparticles Physics*, vol. 13, pp. 45-50, 2000.
- [6] J. Edsjö et al., «Neutrinos from cosmic ray interactions in the Sun,» *arXiv:1704.02892*, 2017.
- [7] C. Argüelles et al., «Solar Atmospheric Neutrinos and the Sensitivity Floor for Solar Dark Matter Annihilation Searches,» *arXiv:1703.07798v1*.
- [8] K. Ng et al., «Solar Atmospheric Neutrinos: A New Neutrino Floor for Dark Matter Searches,» *arXiv:1703.10280v1*.
- [9] M. Masip, «High energy neutrinos from the Sun,» *arXiv:1706.01290 [hep-ph]*.
- [10] G. Ingelman and M. Thunman, «High Energy Neutrino Production by Cosmic Ray Interactions in the Sun,» *Physical Review D*, vol. 54, pp. 4385-4392, 1996.
- [11] J. Vernazza, E. Avrett and R. Loeser, «Structure of the solar chromosphere. III - Models of the EUV brightness components of the quiet-sun,» *Astrophysical Journal Supplement Series*, vol. 45, pp. 635-725, 1981.
- [12] J. Fontenla, K. Balasubramaniam and J. Harder, «Semiempirical models of the solar atmosphere. The quiet sun low chromosphere at moderate resolution.,» *Astrophysical Journal*, vol. 667, n° 2, p. 1243, 2007.
- [13] J. Christensen, *Lecture Notes on Stellar Structure and Evolution*, Institut for Fysik og Astronomi, Aarhus Universitet, 2008.
- [14] G. Feldman and R. Cousins, «Unified approach to the classical statistical analysis of small signals,» *Physical Review D*, vol. 57, p. 3873, 1998.
- [15] G. Hill and K. Rawlins, «Unbiased cut selection for optimal upper limits in neutrino detectors: the model rejection potential technique,» *Astroparticle Physics*, vol. 19, n° 3, pp. 393-402, 2003.

- [16] N. F. Bell and . K. Petraki, «Enhanced neutrino signals from dark matter annihilation in the Sun via metastable mediators,» *JCAP*, vol. 04, n° 003, 2011.
- [17] M. Ardid et al., «Constraining Secluded Dark Matter models with the public data from the 79-string IceCube search for dark matter in the Sun,» *Journal of Cosmology and Astroparticle Physics*, vol. 2017, 2017.
- [18] A. Ibarra, M. Totzauer and S. Wild, «Higher order dark matter annihilations in the Sun and implications for IceCube,» *JCAP*, vol. 04, p. 012, 2014.
- [19] M. Aartsen et al., «Search for dark matter annihilations in the Sun with the 79-string IceCube detector,» *Physical Review Letters*, vol. 110, p. 131302, 2013.
- [20] C. Amole et al., «Dark Matter Search Results from the PICO-2L C3F8 Bubble Chamber,» *Physical Review Letters*, vol. 114, 2015.
- [21] C. Amole et al., «Dark matter search results from the PICO-60 CF3I bubble chamber,» *Physical Review D*, vol. 93, p. 050214, 2016.
- [22] C. Amole et al., «Improved dark matter search results from PICO-2L Run 2,» *Physical Review D*, vol. 93, p. 061101(R), 2016.
- [23] C. Amole et al., «Dark Matter Search Results from the PICO-60 C3F8 Bubble Chamber,» *Phys. Rev. Lett.*, vol. 118, n° 251301, 2017.
- [24] S. Adrián-Martínez et al., «Letter of intent for KM3NeT 2.0,» *J. Phys. G*, vol. 43, n° 084001, 2016.

Combined Search for Neutrinos from Dark Matter Annihilation in the Galactic Center using IceCube and ANTARES

The IceCube[†] and ANTARES Collaborations

[†]http://icecube.wisc.edu/collaboration/authors/icrc17_icecube

E-mail: juaguila@ulb.ac.be

Neutrino telescopes have searched for self-annihilating dark matter in the Galactic Halo and placed stern limits on the dark matter self-annihilation cross section $\langle\sigma v\rangle$ for dark matter particle masses above 30 TeV. To date, the most stringent limit were obtained by the ANTARES neutrino telescope looking at the Galactic Center region for masses $> 100 \text{ GeV}/c^2$ and is closely followed by the limits of the IceCube experiment at lower masses. In this contribution, we present the sensitivities of a future combined search for dark matter in the Milky Way using data from both experiments. From the IceCube experiment, data from 2012 to 2015 with the complete 86-strings detector were selected, while from ANTARES the data sample collected from 2007 to 2015 have been used. The analysis considered dark matter with particle masses ranging from 50 to 1000 GeV/c^2 . We used the annihilation into $\tau\bar{\tau}$ as a benchmark to explore the potential gain by combining the two experiments using a common likelihood framework.

Corresponding authors: J. A. Aguilar^{*1}, N. Iovine¹, C. Tönnis², J. D. Zornoza³

¹ *Université Libre de Bruxelles*

² *Sungkyunkwan University*

³ *IFIC - Instituto de Física Corpuscular*

*35th International Cosmic Ray Conference - ICRC217-
10-20 July, 2017
Bexco, Busan, Korea*

*Speaker.

1. Introduction

Astrophysical observations provide strong evidence for the existence of dark matter in the Universe, however its nature remains unknown. One of the most popular hypotheses for dark matter is that it is made up of non-baryonic particles called WIMP that are non-relativistic, electromagnetically neutral and interacting only via a weak interaction. According to observational evidence, the galaxies are embedded in a halo of thermal relic density of dark matter from the early Universe. The high density of dark matter particles at the center of galaxies, for example in our Milky Way, can contribute to the annihilation of WIMPs producing secondary particles such as high energy neutrinos.

Limits on WIMP dark matter annihilation cross-section have already been set by neutrino detectors such as IceCube [1] and ANTARES [2]. The purpose of this analysis is to combine the data of the two neutrino detectors in the form of probability density function of the two neutrino detectors for the search of neutrinos from dark matter annihilation in the Galactic Center (GC). Another goal of this work is to understand the differences in the approaches taken by Antares and IceCube for this kind of analysis.

2. The IceCube and ANTARES neutrino telescopes

Deep under-water/ice neutrino telescopes follow a similar detection principle. Given the low interaction cross-section of neutrinos, a large volume of target material is required which is achieved by placing a sparse array of photodetectors in deep, dark, and transparent environments such as the sea or the Antarctic ice. The photodetectors will record the Cherenkov emission induced by the secondary particles produced in the deep-inelastic scattering (DIS) interaction of a neutrino with a nucleon of the surrounding medium. The main objective of neutrino telescopes is the detection of astrophysical neutrinos produced close to the cosmic ray sources. However, given the versatility of these experiments they can be used to search for dark matter signatures in an indirect fashion.

The main background contribution of neutrino telescopes comes from atmospheric muons and atmospheric neutrinos. These particles are produced by the interaction of cosmic rays with the higher layers of our atmosphere. Atmospheric muons trigger the detectors more than 6 orders of magnitude more often than atmospheric neutrinos. For up-going directions, the Earth acts as a shield against atmospheric muons. As a consequence, declination corresponding to angles between $0^\circ - 90^\circ$ are less background dominated in the IceCube detector. For ANTARES, declination below -47° are less background dominated since they are always below the horizon of the detector. Declination between -47° and 47° are below the horizon for part of the sidereal day.

2.1 IceCube

IceCube is a cubic-kilometer neutrino observatory located at the South Pole [3] between depths of 1,450 m and 2,450 m and was completed in 2010. The IceCube observatory consists of an array of 5,160 digital optical modules (DOMs) attached to vertical strings placed in 86 boreholes. The reconstruction of the direction, energy and flavor of the neutrinos relies on the optical detection of Cherenkov radiation emitted by charged particles produced in the interactions of neutrinos in the

surrounding ice or the nearby bedrock. In the center of the detector, eight strings are deployed in a more compact way, forming the DeepCore subdetector. This denser configuration extends the detection of neutrinos to energies below 100 GeV.

For this analysis, we use the IceCube data selection developed in the course of the Galactic Center WIMP search analysis [4]. This data sample consists of 1007 days of track-like events compatible with ν_μ signatures taken with the 86-strings configuration from the 15th of May 2012 to 18th of May 2015. Being located at the South Pole, IceCube observes the Galactic Center in the Southern Hemisphere where the background is dominated by atmospheric muons. The selection uses a veto-technique to reduce the level of atmospheric muons by seven orders of magnitude. Details of the event selection can be found in [4]. The total number of events in our sample is 22,553 events.

2.2 ANTARES

The ANTARES telescope is an underwater Cherenkov detector located in the Mediterranean sea, about 40 km from Toulon at depth of roughly 2500 m [5]. ANTARES is a smaller array consisting of 885 optical modules (OM) placed along 12 lines of 350 meters each, spread over a surface of 0.1 km² on the seabed and kept vertical by buoys located at their top. In this work, we consider a data sample corresponding to a total lifetime of 2101.6 days, which corresponds to the actual ANTARES uptime from 2007 to 2015 [6]. The ANTARES detector uses two different reconstruction algorithms depending on the deposited energy of the events: a single line reconstruction for events below 100 GeV and multi-line reconstruction for energies over 100 GeV. The total number of events in this sample is 595 events. Despite its smaller scale compared to IceCube, ANTARES has a privileged view of the Galactic Center as it can use the Earth to block the main contribution of the atmospheric background and therefore no veto is necessary.

3. Dark Matter Annihilation Flux

The expected neutrino flux to be observed in neutrino telescopes from dark matter annihilation is given by [7]

$$\frac{d\phi_\nu(\Psi)}{dA d\Omega dt dE} = \frac{\langle\sigma_A v\rangle}{2} \frac{J_a(\Psi)}{4\pi m_\chi^2} \frac{dN_\nu}{dE}, \quad (3.1)$$

where m_χ is the mass of the WIMP, $\langle\sigma_A v\rangle$ is the WIMPs thermally-averaged annihilation cross-section and dN_ν/dE is the neutrino energy spectrum per annihilating WIMP pair. $J_a(\Psi)$ is the integrated J-factor defined as the integral of the squared dark matter density along the line-of-sight

$$J_a(\Psi) = \int_0^{l_{max}} \rho_\chi^2 \left(\sqrt{R_{sc}^2 - 2lR_{sc}\cos(\Psi) + l^2} \right) dl, \quad (3.2)$$

where Ψ denotes the opening angle to the Galactic Center, R_{sc} is the radius of the solar circle ($R_s \simeq 8.5$ kpc), and ρ_χ is the dark matter density profile. The quantity l is the distance along the line-of-sight and the upper integration limit l_{max} is a quantity which depends on the radius of the Galactic Halo R_{halo} and can be expressed as

$$l_{max} = \sqrt{R_{halo}^2 - \sin^2\Psi R_{sc}^2} + R_{sc} \cos\Psi . \quad (3.3)$$

The radius of the Galactic Halo is chosen to be the radius of the Milky Way $R_{halo} = 50$ kpc and Ψ is the angular distance from the Galactic Center. For this analysis, we used the Navarro-Frenk-White (NFW) dark matter profile

$$\rho_{\chi}(r) = \frac{\rho_0}{\frac{r}{r_s} \left(1 + \frac{r}{r_s}\right)^2} , \quad (3.4)$$

where the parameters to model the matter distribution in the Milky Way are defined in [8], with r_s being the scale radius and ρ_0 the characteristic dark matter density. From these ingredients, it is possible to derive the astrophysical J-factor as a function of Ψ , which is shown in fig. 1 (left).

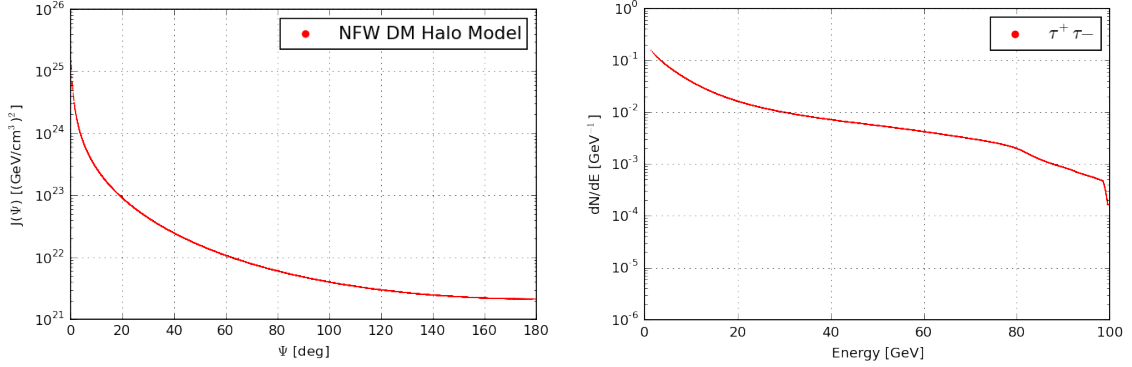


Figure 1: Left: J-factor as a function of the opening angle Ψ calculated for the NFW halo model with the parametrisation found in [8]. **Right :** Neutrino energy spectrum at Earth for the annihilation of WIMP particle of $100 \text{ GeV}/c^2$ mass with ν_{μ} in the final state through the $\tau^+\tau^-$ annihilation channels.

In the following paragraphs, we will focus on the decay of WIMP particles via the $\tau^+\tau^-$ annihilation channel as a benchmark of the analysis for WIMP masses ranging from $50 \text{ GeV}/c^2$ to $1000 \text{ GeV}/c^2$ where the sensitivity of both experiments is comparable. At higher masses, the ANTARES telescope dominates since the effective volume scales with the range of the resulting muon, while the veto-technique of IceCube is beneficial at lower masses. A 100% branching ratio into the $\tau^+\tau^-$ decay channel is assumed. The average neutrino spectra per annihilation process (dN/dE) for these masses and $\tau^+\tau^-$ decay channel were computed using PYTHIA simulation package [9] and are shown in Fig.1 (right).

4. Analysis Method

A binned maximum likelihood method with the two-component mixture model is performed for all annihilation channels assuming WIMP masses ranging from 50 to $1000 \text{ GeV}/c^2$. The first step is to determine the probability density functions (PDFs) of the signal as well as of the background for each experiment. For IceCube, the PDFs used consist of 2-dimensional distributions in right ascension and declination. IceCube PDFs use 12 bins for a band covering $[-2, 2]$ radians

in declination and 10 bins in the full range of right ascension $[-2\pi, 2\pi]$ (see Fig.2). As already mentioned, at low masses ANTARES only reconstructs events using single-line events where the azimuth estimate is not possible. For WIMP masses between 500 and 1000 GeV/c^2 , the multiline reconstruction was used. In both case, PDFs are 1-dimensional distributions of the opening angle Ψ with respect to the Galactic Center (see Fig. 3). The idea of the likelihood analysis is to compare the data to the shapes of the expected signal and the background.

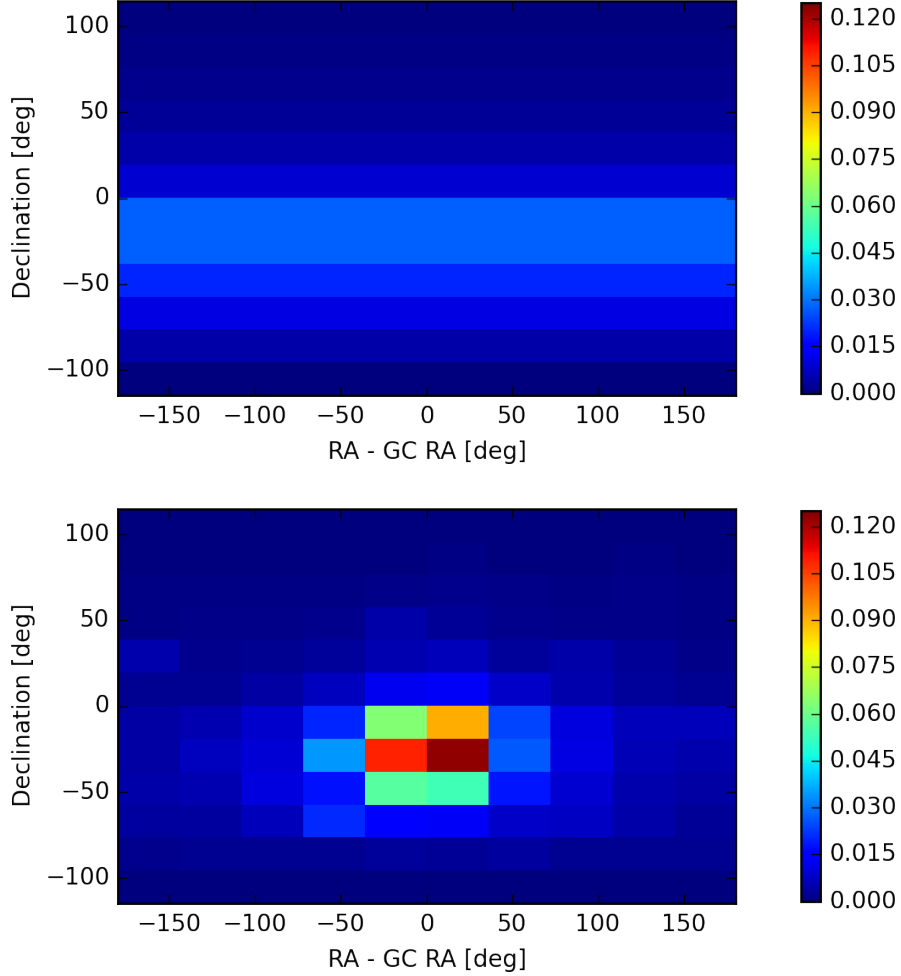


Figure 2: Top: Normalized background PDF of the IceCube sample. Bottom: Normalized signal PDF for the annihilation of 100 GeV/c^2 WIMP particle into the $\tau^+\tau^-$ channel.

The binned likelihood method used in this analysis is defined as

$$\mathcal{L}(\mu) = \prod_{bin_i=bin_{min}}^{bin_{max}} \text{Poisson}(n_{obs}(bin_i) | n_{obs}^{tot} f(bin_i | \mu)) , \quad (4.1)$$

where the parameter to minimize, μ , is the ratio of the number of signal events over the total number of background events in the sample n_{obs}^{tot} . The method compares the observed number of events in a given bin i , $n_{obs}(bin_i)$, with the expectations, $n_{obs}^{tot} f(bin_i | \mu)$, where

$$f(\text{bin}_i|\mu) = \mu f_s(\text{bin}_i) + (1 - \mu) f_{bg}, \quad (4.2)$$

is the fraction of events in the bin i , with f_s and f_{bg} being the signal and the background density distributions shown in Fig. 2 and Fig. 3. In the case of a combined analysis, two likelihoods are combined in a single $\mathcal{L}_{comb}(\mu)$ defined as

$$\mathcal{L}_{comb}(\mu) = \prod_{k=0}^2 \mathcal{L}_k(\mu_k), \quad (4.3)$$

where $k = 0$ represents the ANTARES likelihood and $k = 1$ the IceCube likelihood. Each detector has a signal to background ratio given by $\mu_k = w_k \mu$ where the weight w_k is calculated by taking into account the relative expected number of signal events in each detector, and the relative number of background events in each sample.

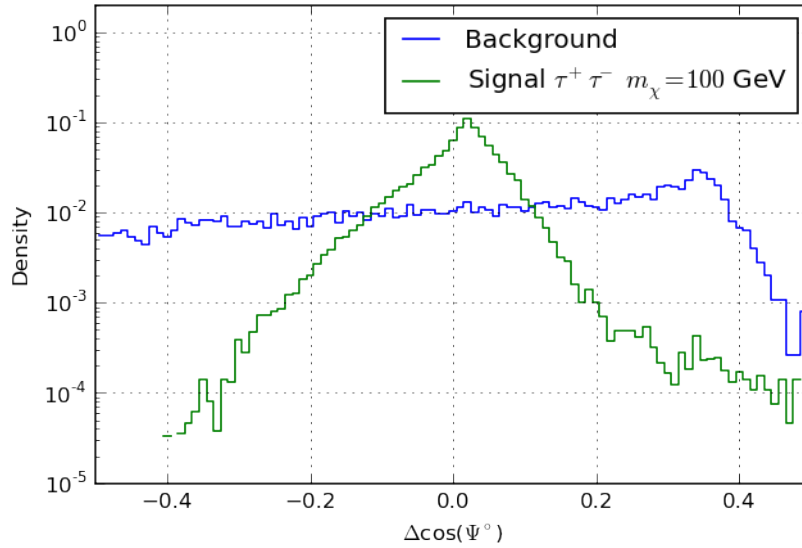


Figure 3: The blue line shows the normalised background PDF of the ANTARES sample, while the green line is the normalised signal PDF for WIMP particles of $100 \text{ GeV}/c^2$ mass that annihilate into via the $\tau^+\tau^-$ channel.

The best estimate of the signal fraction is obtained by minimizing $-\log \mathcal{L}_{comb}(\mu)$. If this value is consistent with zero, the upper limit on the signal fraction, $\mu_{90\%}$, is estimated by determining the 90% confidence interval using the Feldman-Cousins approach [10]. The signal fraction can be linked to $\langle \sigma_A v \rangle$ using the estimated number of signal events for the specific dark matter signal (mass, channel and halo profile). The upper limit on $\langle \sigma_A v \rangle$ for background events only is then calculated by generating a pseudo-experiments sample of 100,000 events and by determining the p-value for the value μ found in the data. We chose to quote the sensitivity as the median value of the 90% upper limits obtained.

5. Results and discussion

The sensitivity to $\langle\sigma_{A\nu}\rangle$ for the combined analysis of IceCube and ANTARES is shown in Fig.4. The results show an improvement of the sensitivity in the energy range of 65 to 1000 GeV/ c^2 when compared to the individual results of both IceCube and ANTARES. This analysis opens the possibility to explore additional channels ($b\bar{b}$, W^+W^- , $\nu_\mu\nu_\mu$, $\mu\bar{\mu}$ and $\tau\bar{\tau}$) and halo profiles in order to set the best limits for a combination of results from all neutrino telescopes.

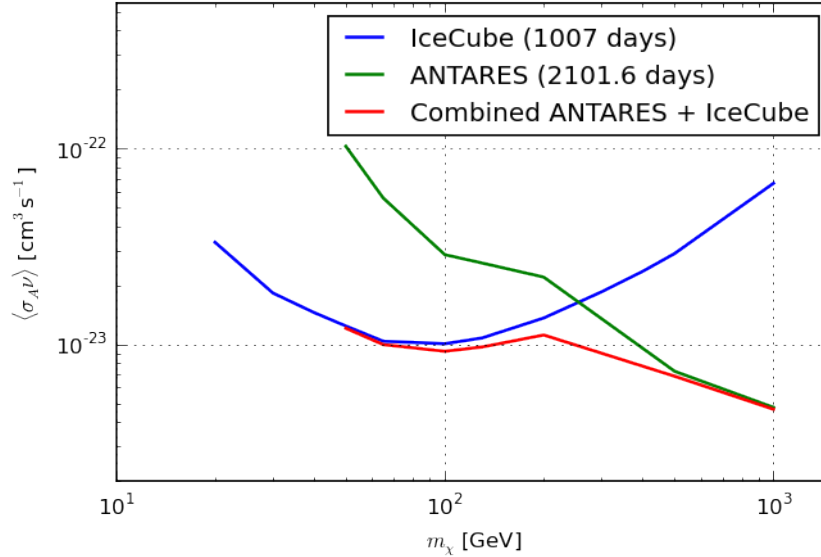


Figure 4: Preliminary plot of the sensitivities obtained for 2101.6 days of ANTARES data (green), 1007 days of IceCube data (blue) and the combination of both experiment (red).

References

- [1] **IceCube** Collaboration, M.G. Aartsen et al., *EPJ C* **75** (2015) 10, 492.
- [2] **ANTARES** Collaboration, S. Adrian et al., *J. Cosmol. Astropart. Phys.* **10** (2015) 068.
- [3] **IceCube** Collaboration, M.G. Aartsen et al., *JINST* **12** (2017) P03012.
- [4] **IceCube** Collaboration, M.G. Aartsen et al., hep-ex/1705.08103.
- [5] **ANTARES** Collaboration, M. Ageron et al., *Nuclear Instruments and Methods in Physics Research Section A: Accelerators, Spectrometers, Detectors and Associated Equipment* **656** (2011) 011.
- [6] **ANTARES** Collaboration, A. Albert et al., *Physics Letters B* **769** (2017) 249.
- [7] H. Yüksel, S. Horiuchi, J. F. Beacom, and S. Ando *Physical Review D* **769** (2017) 249.
- [8] F. Nesti, P. Salucci, *JCAP* **07** (2013) 016.
- [9] T. Sjöstrand, S. Mrenna, and P. Skand, *JHEP* **05** (2006) 026.
- [10] G.J. Feldman, R.D. Cousins, *Phys.Rev.* **D57** (1998).

Indirect searches for dark matter with the ANTARES neutrino telescope

Christoph Tönnis*, on behalf of the ANTARES Collab.

IFIC - Instituto de Física Corpuscular,

Universitat de València–CSIC,

E-46100 Valencia, Spain

Department of Physics,

Sungkyunkwan University,

Seobu 16419, Suwon, South Korea

E-mail: Christoph.toennis@gmx.de

One of the major purposes of the ANTARES neutrino telescope is the indirect search for dark matter. The ANTARES detector is located on the bottom of the Mediterranean Sea, 40 km off the southern French coast. In this talk the results of the search for dark matter signals from the Sun, the Galactic Center and the Earth core, produced with different analysis methods, will be presented. There are various advantages in indirect searches with neutrino telescopes when comparing to other experiments. The analysis for the Sun puts good limits on the spin-dependent scattering cross section between dark matter and hydrogen and the limits presented for the Galactic Center are the most stringent of all indirect detection experiments for WIMP masses above 30 TeV.

35th International Cosmic Ray Conference — ICRC2017

10–20 July, 2017

Bexco, Busan, Korea

*Speaker.

1. Introduction

The ANTARES detector, located 40 km off the shore of Toulon in southern France 2500 m below the surface of the Mediterranean sea, is a neutrino detector, which uses the sea water as its detector medium. It consists of 12, 450 m long, lines of electro–optical cable, each installed in the ocean floor and held up by a buoy. Every line is equipped with 25 so–called storeys, each containing 3 optical modules. An optical module is a 17–inch borosilicate sphere containing a 10–inch photomultiplier tube (PMT) of the type Hamamatsu R7081-20 and the electronics to control it. This makes a total of 900 PMTs in the whole detector.

One of the main physics goals of neutrino telescopes is the indirect search for dark matter [1, 2]. The concept behind the search is that dark matter particle accumulate in massive objects either primordially or via scattering with the matter of the objects and annihilate inside of them, producing pairs of standard model particles. These particles then decay further, producing neutrinos in these secondary processes. The results of three of these searches, one for annihilations in the Sun, one for annihilations in the Earth and one for annihilations in the Milky Way, are presented in this proceeding. Further analyses for secluded dark matter [3] have been performed using ANTARES.

The currently most prevalent hypothesis on dark matter is that it is composed of weakly interacting massive particles (WIMPs) that form halos in which galaxies are embedded. As candidates for the WIMP typically supersymmetric particles are considered.

In the search for dark matter in the Milky Way the extension of the source had to be taken into account. This extension for searches looking for annihilations is expressed by the so–called J-Factor. The J-Factor is the squared dark matter density of the source integrated over the line of sight. It is calculated by

$$J(\theta) = \int_0^{l_{\max}} \frac{\rho_{\text{DM}}^2 \left(\sqrt{R_{\text{SC}}^2 - 2lR_{\text{SC}} \cos(\theta) + l^2} \right)}{R_{\text{SC}} \rho_{\text{SC,DM}}^2} dl, \quad (1.1)$$

where R_{SC} and ρ_{SC} are the scaling radius and density. The J-Factor is also needed to relate the neutrino flux $\frac{d\phi_{\nu}}{dE}$ to the thermally averaged annihilation cross–section $\langle \sigma v \rangle$:

$$\frac{d\phi_{\nu}}{dE} = \frac{\langle \sigma v \rangle}{2} J_{\Delta\Omega} \frac{R_{\text{SC}} \rho_{\text{SC}}^2}{4\pi m_{\chi}^2} \frac{dN_{\nu}}{dE}, \quad (1.2)$$

where $J_{\Delta\Omega}$ is the J-Factor integrated over the observation window $\Delta\Omega$, m_{χ} is the WIMP mass and $\frac{dN_{\nu}}{dE}$ is the expected signal neutrino spectrum. For the dark matter halo profile ρ_{DM} the NFW profile was considered with parameters taken from [5].

The Sun, however, is sufficiently small to be considered a point–like source, so the source extension does not have to be taken into account. When limits on dark matter model parameters are calculated an equilibrium between the accumulation of dark matter in the Sun and their annihilation is assumed. This allows to convert limits and sensitivities in terms of neutrino fluxes to spin dependent and spin independent scattering cross–section limits (σ_{SD}^p and σ_{SI}) assuming a Maxwellian velocity distribution of the WIMPs with a root mean square velocity of $270 \text{ km} \cdot \text{s}^{-1}$ and a local dark matter density of $0.3 \text{ GeV} \cdot \text{cm}^{-3}$ [7].

For the Earth no equilibrium can be asserted and instead a value for the thermally averaged annihilation cross section in the Earth, $\langle\sigma_A v\rangle_{\text{Earth}}$, is assumed.

To remain independent of particle dark matter models, limits are calculated using so-called annihilation channels. An annihilation channel is the assumption that all WIMP annihilations initially lead to the same pair of standard model particles. There are five channels that were considered:

$$\text{DM} + \text{DM} \rightarrow b\bar{b}, W^+W^-, \tau^+\tau^-, \mu^+\mu^-, \nu\bar{\nu} \quad (1.3)$$

The $\nu\bar{\nu}$ and $\mu^+\mu^-$ channel have not been considered for the search for WIMP annihilations in the Sun and the Earth to simplify the analysis. The $\tau^+\tau^-$ channel is most commonly used as a benchmark for comparisons between experiments. When the expected neutrino signal spectra are calculated for the Sun, the absorption of neutrinos in the solar plasma has to be taken into account. In both cases neutrino oscillations were accounted for in the calculations, which were carried out using the WIMPSIM code [8] for the Sun and using the code described in [9] for the Milky Way.

The sensitivities and limits are then converted to neutrino fluxes using a quantity referred to as acceptance. The acceptance is defined as:

$$\text{Acc}(m_{\text{WIMP}}, \text{Ch}) = \int_{E_{\text{th}}}^{m_{\text{WIMP}}} A_{\text{eff}}(E_{\nu_\mu}) \left. \frac{dN_{\nu_\mu}}{dE_{\nu_\mu}} \right|_{\text{Det,Ch}} dE_{\nu_\mu} + \int_{E_{\text{th}}}^{m_{\text{WIMP}}} A_{\text{eff}}(E_{\bar{\nu}_\mu}) \left. \frac{dN_{\bar{\nu}_\mu}}{dE_{\bar{\nu}_\mu}} \right|_{\text{Det,Ch}} dE_{\bar{\nu}_\mu}, \quad (1.4)$$

where $A_{\text{eff}}(E_{\nu_\mu})$ is the effective area for the muon neutrino energy E_{ν_μ} or muon antineutrino energy $E_{\bar{\nu}_\mu}$, $\left. \frac{dN_{\nu_\mu}}{dE_{\nu_\mu}} \right|_{\text{Det,Ch}}$ is the signal neutrino spectrum at the position of the detector for one particular annihilation channel Ch listed in equation 1.3, E_{th} is the energy threshold of the detector and m_{WIMP} is the WIMP mass. The effective area, which is the size of a 100%-efficient detector giving the same number of events, is calculated from the Monte Carlo simulation. The 90% C.L. limits and sensitivities on the fluxes are then calculated by:

$$\bar{\Phi}_{\nu_\mu + \bar{\nu}_\mu, 90\%} = \frac{\bar{\mu}_{\nu_\mu + \bar{\nu}_\mu, 90\%}(m_{\text{WIMP}})}{\text{Acc}(m_{\text{WIMP}}) \cdot T_{\text{live}}}, \quad (1.5)$$

where $\bar{\mu}_{\nu_\mu + \bar{\nu}_\mu, 90\%}$ is the 90% C.I. sensitivity or limit and T_{live} is the total live time of the detector.

For the analyses presented here a maximum likelihood algorithm was used. This algorithm searches for signals using a likelihood function. For this analysis the likelihood has the form:

$$\log_{10}(\mathcal{L}(n_s)) = \sum_{i=1}^{N_{\text{tot}}} \log_{10}(n_s S(\psi_i, p_i, q_i) + N_{\text{tot}} B(\psi_i, p_i, q_i)) - n_s - N_{\text{tot}}. \quad (1.6)$$

N_{tot} is the total number of reconstructed events, n_s is the supposed number of signal events, ψ_i is the angular position of the i_{th} event, p_i and q_i are additional event parameters like the reconstruction quality or the estimated neutrino energy. S represents the ANTARES point spread function (PSF) and B is a function that represents the behaviour of the background.

Pseudo experiments are then used to study the behaviour of the likelihood function. A pseudo experiment is a simulated event distribution, generated from a background estimate including a given number of fake signal events. For each pseudo experiment the likelihood function is optimised with regards to n_s and a parameter called test statistic is calculated:

$$TS = \log_{10} \left(\frac{L(n_s)}{L(0)} \right). \quad (1.7)$$

The sensitivities in terms of detected signal events $\mu_{90\%}$ are calculated from the overlap of the distribution of TS values for different numbers of inserted fake signal events. Upper limits on the number of signal events are then calculated comparing the TS value of the actual data to the TS distributions of pseudo experiments.

2. Search in the Earth

For the search for Dark matter annihilations in the Earth data recorded from 2007 to 2012 have been used. Upper limits at 90% C.L. on the WIMP annihilation rate in the Earth and the spin independent scattering cross-section of WIMPs to nucleons were calculated for three annihilation channels. A comparison of these limits to the results of other experiments is presented in Figure 1. For masses of the WIMP close to the mass of iron nuclei ($50\text{GeV}/c^2$), the obtained limits are more stringent than those obtained by other indirect searches.

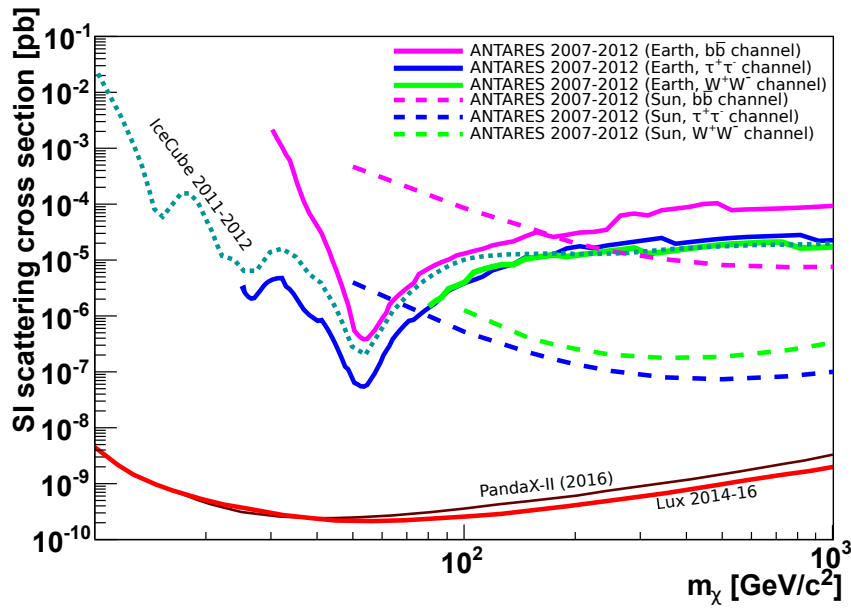


Figure 1: Limits on the spin-independent WIMP–nucleon scattering cross-section as a function of WIMP mass assuming $\langle \sigma_{AV} \rangle_{\text{Earth}} = 3 \cdot 10^{-26} \text{cm}^3 \text{s}^{-1}$. Results from IceCube-79 [10], PandaX-II [11] and LUX [12] are shown as well.

3. Search in the Sun

The indirect search for dark matter in the Sun was performed using a dataset that was collected between 2007 and 2012. In that dataset no significant excess was found and therefore limits on the spin dependent and spin independent scattering cross-section were set. In Figure 2 the limits on the spin dependent scattering cross-section are compared to the results from other experiments. At low

WIMP masses the SuperKamiokande experiment provides the most stringent limits intersecting with the limits from neutrino telescopes at 100 GeV. Above that the IceCube experiment generates the lowest limits. However the comparison to the ANTARES limits is extremely close considering the enormous difference in size between the experiments. This is possible because of the much better angular resolution of ANTARES due to the smaller amount of scattering in water compared to ice.

Since direct detection experiments are not designed to be sensitive to σ_{SD}^p they can usually not compete with neutrino experiments for this parameter. Only the bubble chamber experiment PICO can provide limits in a similar order of magnitude because it uses a target material with a high density of unpaired spin.

In figure 3 the spin independent scattering cross section limit is shown in comparison to other experiments. The spin independent scattering is dependent on the abundance of helium in the Sun, whilst the spin dependent scattering depends on the abundance of hydrogen. Since helium is much less prevalent than hydrogen in the Sun the spin independent cross-section limits are much less stringent than those shown in figure 2. Direct detection experiments, being designed for a high sensitivity to spin independent scattering, provide much lower limits in comparison to those from neutrino experiments.

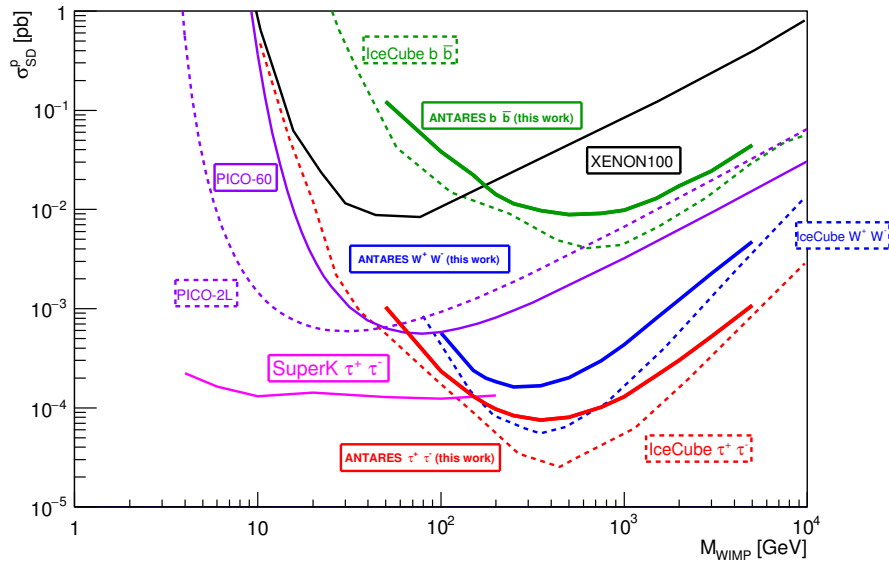


Figure 2: Limits on the spin-dependent WIMP–nucleon scattering cross-section as a function of WIMP mass for the $b\bar{b}$, $\tau^+\tau^-$ and W^+W^- channels. Limits given by other experiments are also shown: IceCube [13], PICO-60 [15], PICO-2L [16], SuperK [17], XENON100 [18].

The comparison to IceCube in figure 3 is much more favourable since the limits shown there did only use muon tracks and a smaller data sample as the most recent IceCube publication for this type of search [13], which did not include limits on the spin independent cross-section.

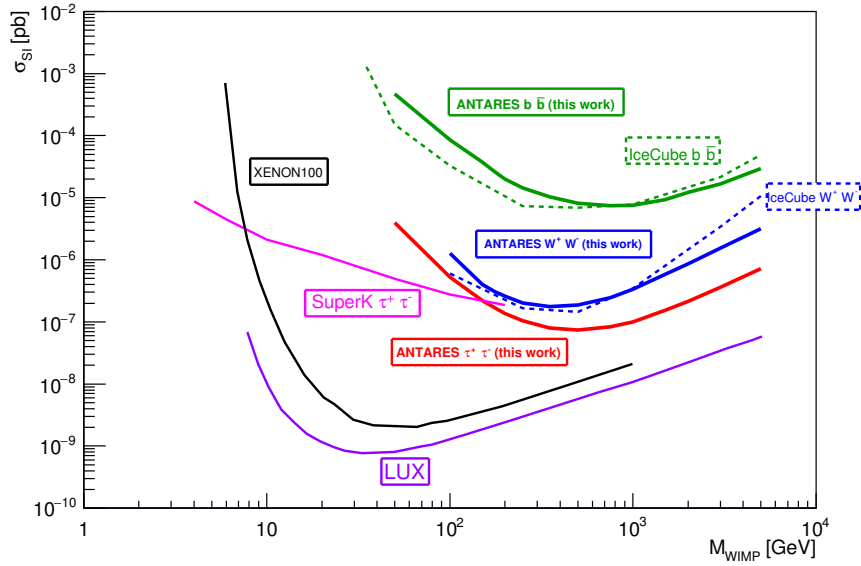


Figure 3: Limits on the spin-independent WIMP–nucleon scattering cross-section as a function of WIMP mass for the different channels considered. Limits given by other experiments are also shown: IceCube [14], SuperK [17], LUX [19], XENON100 [20].

4. Search in the Galactic Centre

For the search in the Galactic Centre a larger dataset, containing events from 2007 to 2015, has been used. Just as in the case of the Sun no significant excess above the expected background has been found and limits on the thermally averaged annihilation cross-section were set.

The limits on $\langle \sigma v \rangle$ are compared to those from other experiments in figure 4. For all WIMP masses above 100 GeV the limits from ANTARES supersede those from IceCube by more than one order of magnitude. This comparison is favourable since ANTARES has a good visibility towards the Galactic Centre, whilst IceCube needs to use a veto to exclude atmospheric muons. This veto reduces the effective area of IceCube, particularly at high energies.

Gamma ray experiments provide the most stringent limits for WIMP masses lower than 30 TeV. Above that the limits from ANTARES are the most stringent. This has to be considered with the caveat that the limits from HESS use the Einasto halo profile, which is less cuspy than the NFW profile used for the ANTARES limit.

5. Conclusions

Despite the much smaller size of ANTARES in comparison to similar experiments competitive limits for the spin dependent scattering cross-section could be provided. Especially positive were the very strong constrains that were set on the thermally averaged annihilation cross-section, that are the currently best limits of all neutrino telescopes and even supersede limits from gamma ray experiments. Further analyses for the Earth and secluded dark matter have been performed as well [3, 4].

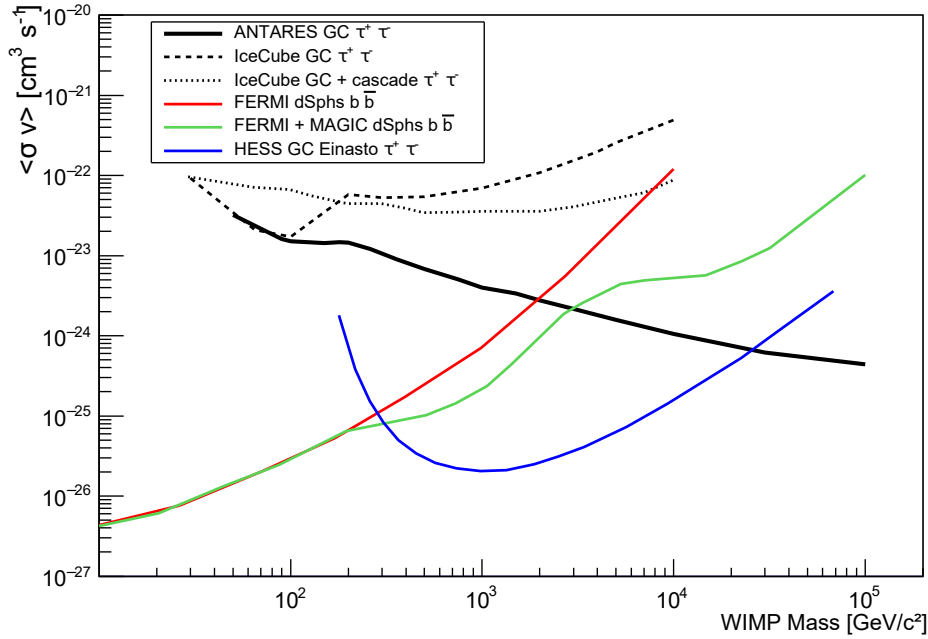


Figure 4: 90% C.L. limits on the thermally averaged annihilation cross-section, $\langle\sigma v\rangle$, as a function of the WIMP mass in comparison to the limits from other experiments [21, 22, 23, 24, 25]. The results from IceCube and ANTARES were obtained with the NFW profile.

References

- [1] M. Klasen, M. Pohl, G. Sigl, *Indirect and direct search for dark matter*, Progress in Particle and Nuclear Physics 85 1 (2015)
- [2] G. Bertone, D. Hooper, J. Silk, *Particle Dark Matter: Evidence, Candidates and Constraints*, Phys. Rep. 405 279 (2005)
- [3] ANTARES Collaboration, S. Adrian-Martinez et al., *A search for Secluded Dark Matter in the Sun with the ANTARES neutrino telescope*, JCAP 05 016 (2016)
- [4] ANTARES Collaboration, A. Albert et al., *Search for dark matter annihilation in the earth using the ANTARES neutrino telescope*, Phys. of the Dark Univ. 16 41 (2017)
- [5] F. Nesti, P. Salucci, *The Dark Matter Halo of the Milky Way*, AD 2013, JCAP 07 016 (2013)
- [6] Paul J. McMillan, *The mass distribution and gravitational potential of the Milky Way*, MNRAS 414 2446 (2015)
- [7] G. Wikström, J. Edsjö, *Limits on the WIMP-nucleon scattering cross-section from neutrino telescopes*, JCAP 0904 009 (2009)
- [8] M. Blennow, J. Edsjo, T. Ohlsson, *Neutrinos from WIMP Annihilations obtained using a Full Three-Flavor Monte Carlo Approach*, JCAP 0801 021 (2008)
- [9] M. Cirelli et al., *PPPC 4 DM ID: A Poor Particle Physicist Cookbook for Dark Matter Indirect Detection*, JCAP 1103 051 (2011)

- [10] IceCube Collaboration, M. G. Aartsen et al., *First search for dark matter annihilations in the Earth with the IceCube Detector*, EPJ C77 82 (2017)
- [11] PandaX-II Collaboration, Andi Tan et al., *Dark Matter Results from First 98.7 Days of Data from the PandaX-II Experiment*, Phys. Rev. Lett. 117 121303 (2016)
- [12] LUX Collaboration, D. S. Akerib et al., *Results from a search for dark matter in the complete LUX exposure*, Phys. Rev. Lett. 118 021303 (2017)
- [13] IceCube Collaboration, M. G. Aartsen et al., *Improved limits on dark matter annihilation in the Sun with the 79-string IceCube detector and implications for supersymmetry*, JCAP 1604 022 (2016)
- [14] IceCube Collaboration, M. G. Aartsen et al., *Search for dark matter annihilations in the Sun with the 79-string IceCube detector*, Phys. Rev. Lett., 110 131302 (2013)
- [15] PICO Collaboration, C. Amole et al., *Dark Matter Search Results from the PICO-60 CF3I Bubble Chamber*, Phys. Rev. D 93 052014 (2016)
- [16] PICO Collaboration, C. Amole et al., *Improved Dark Matter Search Results from PICO-2L Run-2*, Phys. Rev. D 93 061101 (2016)
- [17] Super-Kamiokande Collaboration, K. Choi et al., *Search for Neutrinos from Annihilation of Captured Low-Mass Dark Matter Particles in the Sun by Super-Kamiokande*, Phys. Rev. PRL 114 141301 (2015)
- [18] XENON100 Collaboration, E. Aprile et al., *Limits on spin-dependent WIMP-nucleon cross sections from 225 live days of XENON100 data*, Phys. Rev. Lett. 111 021301 (2013)
- [19] LUX Collaboration, D. S. Akerib et al., *First results from the LUX dark matter experiment at the Sanford Underground Research Facility*, Phys. Rev. Lett. 112 091303 (2014)
- [20] XENON100 Collaboration, E. Aprile et al., *Dark Matter Search Results from 225 Live Days of XENON100 Data*, Phys. Rev. Lett. 109 181301 (2012)
- [21] M. G. Aartsen et al., IceCube Collaboration, *Search for Dark Matter Annihilation in the Galactic Center with IceCube-79*, EPJC 75492 (2015)
- [22] M. G. Aartsen et al., IceCube Collaboration, *All-flavour Search for Neutrinos from Dark Matter Annihilations in the Milky Way with IceCube/DeepCore*, EPJC 76 531 (2016)
- [23] M. Ackermann et al., Fermi-LAT Collaboration, *Searching for Dark Matter Annihilation from Milky Way Dwarf Spheroidal Galaxies with Six Years of Fermi Large Area Telescope Data*, Phys. Rev. Lett. 115 231301 (2015)
- [24] R. Caputo, M. R. Buckley, P. Martin, E. Charles, A. M. Brooks, A. Drlica-Wagner, J. M. Gaskins, M. Wood, *Search for Gamma-ray Emission from Dark Matter Annihilation in the Small Magellanic Cloud with the Fermi Large Area Telescope*, Phys. Rev. D 93 6 062004 (2016)
- [25] H. Abdallah et al., HESS Collaboration, *Search for dark matter annihilations towards the inner Galactic halo from 10 years of observations with H.E.S.S.*, Phys. Rev. Lett. 117 11 111301 (2016)

Search for $\beta > 0.6$ magnetic monopoles with the ANTARES neutrino telescope

Imad El Bojaddaini*

Mohamed I University, Oujda, Morocco

E-mail: elbojaddaini_1990@hotmail.fr

Antoine Kouchner†

APC, Univ Paris Diderot, France

E-mail: kouchner@apc.univ-paris7.fr

The search for magnetic monopoles with the ANTARES neutrino telescope is presented. These hypothetical particles carry only a magnetic charge. They would be created in the primordial Universe within the phase transition corresponding to the spontaneous breaking of the unified gauge group into subgroups, then would be accelerated by the Galactic magnetic fields and reach the Earth. Magnetic monopoles could be detected as highly ionizing particles in neutrino telescopes. This new analysis uses a total live time of 1121 days of the ANTARES detector. No signal above the background expectation from atmospheric muons and neutrinos is observed, and new 90% C.L. upper limits are set on the magnetic monopole flux for velocities $\beta = v/c \geq 0.6$. These limits hold for up-going magnetic monopoles in the mass range $10^{10} \text{ GeV}/c^2 \leq M \leq 10^{14} \text{ GeV}/c^2$.

35th International Cosmic Ray Conference ICRC2017

10-20 July, 2017

Bexco, Busan, Korea

*On behalf of the ANTARES collaboration

†Speaker

1. Introduction

The concept of electric monopole is very familiar in physics although it is known with its more common name "electric charge", because it exists in the form of particles that have positive or negative charges like electrons and protons. Opposite electric charges attract and like charges repel through the interaction of electric fields, which are defined as running from positive to negative. Magnetism seems analogous to electricity, as there exist a magnetic field with a direction defined as running from north to south. However, this analogy breaks down when trying to find the magnetic counterpart of the electric charge, the magnetic monopole (MM). This particle with only one magnetic pole has never been observed, instead, magnets exist only in the form of dipoles with a north and a south end.

The main theory introducing magnetic monopoles was presented by P. A. M. Dirac in 1931 [1]. Indeed, measured electric charges are always found to be integer multiples of the electron charge. This quantization of electric charge is a deep property of Nature without an explanation. Dirac discovered that the existence of magnetic monopoles explains the quantization of the electric charge in the framework of quantum mechanics.

In contrast to Dirac's demonstration of the consistency of magnetic monopoles with quantum mechanics, G. 't Hooft [2] and A. M. Polyakov [3] demonstrated independently in 1974 the necessity of magnetic monopoles in unified gauge theories. Any unified gauge theory in which the group $U(1)$ describing electromagnetism is embedded in a spontaneously broken semisimple gauge group, and electric charge is thus automatically quantized, necessarily contains magnetic monopoles.

While there is no indication of the mass of the Dirac's magnetic monopole, in the context of GUTs the magnetic monopole mass M is related to the mass of the X -boson carrier of the unified interaction ($m_X \sim 10^{15} \text{ GeV}/c^2$), yielding $M \gtrsim m_X/\alpha \simeq 10^{17} \text{ GeV}/c^2$. An object this massive may have been produced only in the very early stages of the Universe after the Big Bang, and if the Universe cooled down to a point that MM creation was no longer energetically possible, perhaps MMs exist and the exponential expansion called inflation just distributed them everywhere. This was one of the motivations for the scenario of the inflationary Universe introduced by Guth [4] which explains the non-abundance of MMs. With the expansion of the Universe, the MM energy decreased, then MMs have been re-accelerated by the galactic magnetic fields. This acceleration process drains energy from the galactic magnetic field. An upper bound on the flux of MMs in the galaxy (called the Parker bound [5]) has been obtained by requiring the rate of this energy loss to be small compared to the time scale on which the galactic field can be regenerated.

Recent searches for magnetic monopoles created through electroweak interactions in the mass range $M < 10 \text{ TeV}$ have been performed by the MoEDAL experiment at CERN. Since no candidates were found, upper limits were established on the MM production cross sections [6].

Neutrino and cosmic ray telescopes such as MACRO [7], Baikal [8], IceCube [9] and Pierre-Auger [10] attempted to detect magnetic monopoles with no positive result so far. The ANTARES Neutrino telescope has found upper limits on MM flux in a result published in [11].

In this paper, a new search for MMs is presented, using five years of the ANTARES detector data collected from 2008 to 2012, and corresponding to 1121 active days of live time.

2. Magnetic monopoles signature

The Earth acts as a shield against all particles except neutrinos. The ANTARES neutrino telescope [12] uses the detection of up-going charged particles as a signature of neutrino interaction in the matter below the detector. The detection of muons in water through Cherenkov light emission allows the determination of their trajectory. This detection technique requires discriminating up-going muons against the much higher flux of down-going atmospheric muons.

Since the ANTARES telescope is sensitive to up-going particles, this reduces the mass range of magnetic monopoles that can be observed. Indeed, the stopping power defined by Ahlen [13] has been used to estimate the energy loss of a monopole when crossing the Earth. However, despite the high energy loss, monopoles would remain relativistic and detectable as up-going events if their mass $M \gtrsim 10^{10} \text{ GeV}/c^2$. On the other hand, the monopole speed depends on the characteristics of the galactic magnetic fields, thus, given some astrophysical considerations, only monopoles with $M \lesssim 10^{14} \text{ GeV}/c^2$ are expected. The limits found in this analysis hold for monopoles with $10^{10} \text{ GeV}/c^2 \lesssim M \lesssim 10^{14} \text{ GeV}/c^2$.

The signature of a magnetic monopole in ANTARES would be similar to that of a high energy muon. MMs would induce the polarization of the medium to allow Cherenkov emission if their velocity exceeds the Cherenkov threshold $\beta_{th} = 1/n \approx 0.74$. In addition, MMs can knock off atomic electrons that can have velocities above Cherenkov threshold, contributing to the total light yield by the so-called δ -rays. The production of these δ -electrons is described by the differential cross-section of Kasama, Yang and Goldhaber KYG [14] or the Mott cross section [15]. Fig. 1 shows the light yield with all these mechanisms compared to that from a minimum ionizing muon.

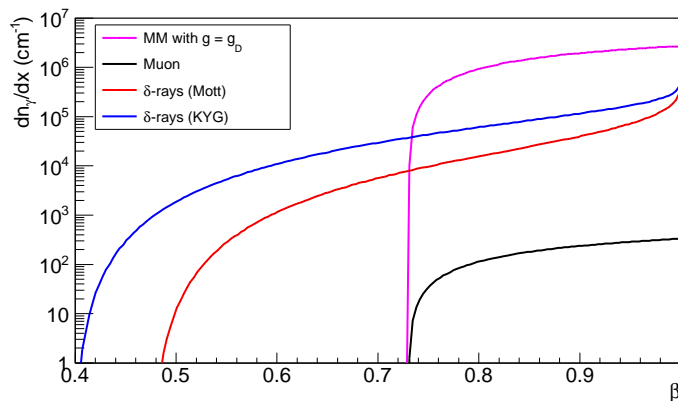


Figure 1: The total number of Cherenkov photons with wavelengths between 300 and 600 nm that are directly produced per centimeter path length by a MM with $g = g_D$, as a function of its velocity (β). The number of photons produced by δ -rays with Mott cross section model [15] and KYG cross section model [14] and by a minimum ionizing muon are also shown.

3. Monte Carlo simulation and reconstruction

MMs are simulated in nine ranges of velocity in the interval $\beta = [0.5945, 0.9950]$ using a

Monte Carlo program based on GEANT3. MM events are generated isotropically over the lower hemisphere of the detector. The propagation and detection of emitted photons is processed inside a virtual cylindrical surface surrounding the instrumented volume around the detector.

The simulation of atmospheric muons is carried out using the generator MUPAGE [16] based on the parametrisation of the angle and energy distributions of muons under-water as a function of the muon bundle multiplicity.

Up-going atmospheric neutrinos from the decay of pions and kaons are simulated using the package GENHEN [17] assuming the model from the Bartol group [18] which does not include the decay of charmed particles.

The analysis presented in this paper is based on a run-by-run Monte Carlo strategy [19], which simulates each run of data individually taking into consideration its actual conditions (e.g. sea water conditions, bioluminescence variability, detector status).

The reconstruction algorithm [20] performs two independent fits: a track fit and a bright-point fit. The former reconstructs particles crossing the detector, while the latter reconstructs showering events, as those induced by the charged current interactions. Both fits minimize the same χ^2 quality function, thus, two parameters defining the quality of these reconstructions are introduced, $t\chi^2$ for the track fit, and $b\chi^2$ for the bright-point fit. Fig. 2 shows the distribution of $t\chi^2$ for atmospheric muons and neutrinos. The search strategy was based on a blind analysis, such as the selection cuts applied are established on Monte Carlo simulation and using a test data sample of about 10% of the total data set. The neutrino distribution represents electron and muon neutrinos for both neutral and charged currents. In order to select data taken in good conditions, some basic quality cuts have been applied.

Event reconstruction has been performed assuming the reconstructed velocity of the particle β_{rec} as a free parameter to be derived by the track fit. This improves the sensitivity for monopoles travelling with $\beta \leq 0.81$.

4. Event selection and optimization

In order to get rid of the bulk of down-going background events, only up-going events are selected. From Fig. 2, one can notice the significant agreement between the simulated atmospheric background and the sample of data. This was achieved by applying the cut $t\chi^2 \leq b\chi^2$ in order to favor the reconstructed tracks rather than showers.

Despite quality cuts, the selected event sample remains dominated by atmospheric muons for low velocities. Additional cuts on the track fit quality parameter are implemented to remove misreconstructed atmospheric muon tracks. The selection of the events was further optimized for different MM velocities. A different event selection was performed for each of the nine bins of β .

The hits from the optical modules belonging to the same storey are summed together to form a track hit. For all velocity bins, the number of storeys with selected track hits N_{hit} is used as a powerful discriminant variable since it refers to the amount of light emitted. A second discriminative variable is introduced to further reduce the background in particular for lower velocities where the light emission is less. This variable named α is defined from a combination of the track fit quality parameter and N_{hit} , and allows to avoid that bright events get cut by the condition applied on the $t\chi^2$ variable. Fig. 3 shows the distribution of α and N_{hit} used in the optimization.

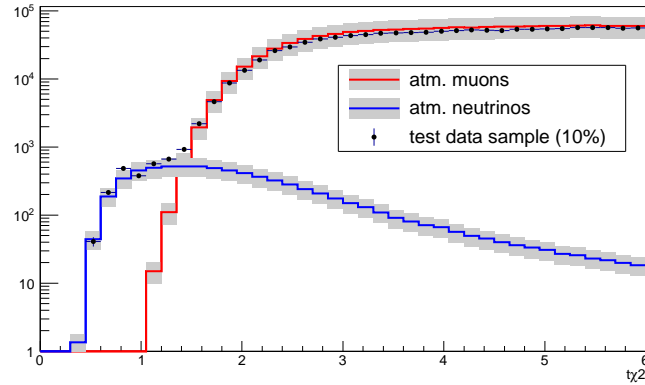


Figure 2: The distribution of $t\chi^2$ for atmospheric muons, atmospheric neutrinos (red and blue histograms, respectively) and data (points with error bars). The systematic uncertainties on the flux of atmospheric muons and neutrinos are represented by error bands. All distributions correspond to events reconstructed as up-going, and the cut $t\chi^2 \leq b\chi^2$ has been applied as it allows to choose tracks rather than showers.

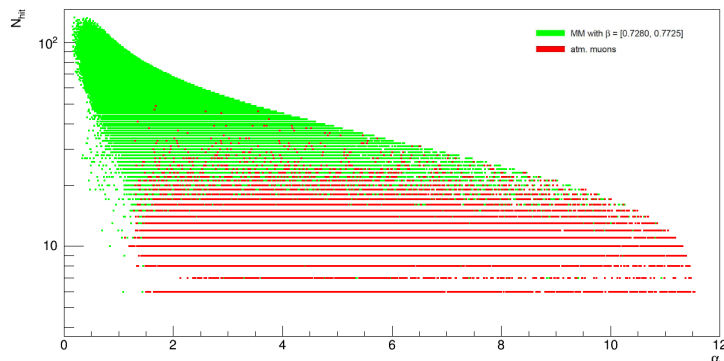


Figure 3: Two-dimensional distribution of α and N_{hit} , for atmospheric muons (red) and MMs (green) simulated in the velocity range $[0.7280, 0.7725]$. The distributions correspond to up-going events with $t\chi^2 \leq b\chi^2$ and $\beta_{rec} = [0.7280, 0.7725]$. No neutrinos survived at this range of β .

5. Uncertainties

Taking into account the statistical uncertainties, an extrapolation of N_{hit} distribution is performed for atmospheric muons in order to compensate the lack of statistics. After fitting the N_{hit} distribution with a Landau type function, the latter is extrapolated to the region of interest for the signal (see Fig. 4). The number of muons remaining after the final cut on N_{hit} is given by the sum of the events remaining from the muon histogram and those remaining from the extrapolated function.

The contribution of atmospheric neutrinos in the calculation of the upper limits is negligible compared to that from atmospheric muons (see Table 1 in the next section). Thus the effect on the neutrino rate due to the detector uncertainties are not considered. Concerning the atmospheric muons, the dominant effect is due to the lack of statistics as described in Fig. 4. It is larger than

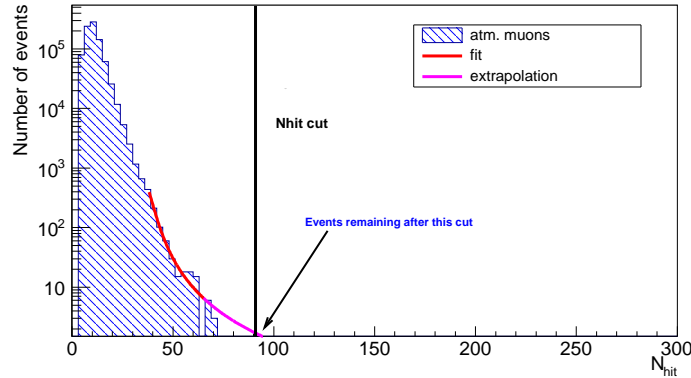


Figure 4: The distribution of N_{hit} for atmospheric muons, extrapolated using a Landau fit function. The contribution of the extrapolation in the total number of events was taken into account in the optimization and the extrapolation uncertainties were computed. For this bin $\beta = [0.8170, 0.8615]$, 1.4 events are found after the cut $N_{hit} \geq 91$.

50% in most cases (see column 3 of Table 1), while the uncertainty on the optical module and the uncertainty on the light absorption and scattering lengths in water yield an overall effect of 35% for muons and 30% for neutrinos [21]. These uncertainties are represented in Fig. 2 by an error band around each histogram.

6. Results

Using the Feldman-Cousins approach [22], the selection cuts are optimized by minimizing the so-called Model Rejection Factor (MRF) [23].

After applying the unblinding on the total set of data collected by ANTARES from 2008 to 2012 that corresponds to 1012 active days live time after extracting the 10% data sample, no significant excess is observed over the atmospheric background expectation and upper limits on MMs flux at 90% C.L. are found and quoted in Table 1, for each bin of β .

In the first five bins, the reconstructed velocity β_{rec} was restricted to be compatible with the range of the MM velocity. In the last bins, β was not reconstructed as it does not contribute to isolate the MM signal.

Fig. 5 represents the ANTARES upper limits found as a function of MM β , and compared to different experiments such as IceCube [9], MACRO [7] and Baikal [8], as well as the previous result from ANTARES [11] and the theoretical Parker bound [5].

7. Conclusion

This paper presented the ANTARES upper limits found with five years of data recorded between 2008 and 2012 and corresponding to 1012 days of live time. This new analysis was based on a Monte Carlo strategy which consists in simulating each run individually, in order to take into account its specific conditions ("run-by-run" simulation).

β range	Selection cuts		Number of atm. muons	Number of atm. neutrinos	Number of obs. events	Flux Upper Limits 90% C.L. ($\text{cm}^{-2} \cdot \text{s}^{-1} \cdot \text{sr}^{-1}$)
	α	N_{hit}				
[0.5945, 0.6390]	< 5.5	≥ 36	1.9 ± 0.8	1.6×10^{-4}	0	5.9×10^{-16}
[0.6390, 0.6835]	< 5.0	≥ 39	0.9 ± 0.5	1.5×10^{-4}	0	3.6×10^{-17}
[0.6835, 0.7280]	< 3.4	≥ 51	0.9 ± 1.0	1.2×10^{-4}	0	2.1×10^{-17}
[0.7280, 0.7725]	< 3.3	≥ 51	1.1 ± 0.5	9.3×10^{-3}	1	9.1×10^{-18}
[0.7725, 0.8170]	< 1.8	≥ 73	0.6 ± 0.4	1.0×10^{-3}	0	4.5×10^{-18}
[0.8170, 0.8615]	< 0.8	≥ 91	1.4 ± 0.9	1.8×10^{-1}	1	4.9×10^{-18}
[0.8615, 0.9060]	< 0.6	≥ 92	1.3 ± 0.8	1.6×10^{-1}		2.5×10^{-18}
[0.9060, 0.9505]	< 0.6	≥ 94	1.2 ± 0.8	1.3×10^{-1}	0	1.8×10^{-18}
[0.9505, 0.9950]	< 0.6	≥ 95	1.2 ± 0.7	1.3×10^{-1}	0	1.5×10^{-18}

Table 1: Results after unblinding of the data (1012 active days live time corresponding to 5 years of data taking). The selection cuts, the number of expected (muons and neutrinos) background and observed events and the upper limits on the flux are presented for each range of velocity (β). The table was divided into two parts to distinguish the first five bins where β_{rec} was assumed as a free parameter from the four bins where $\beta_{rec} = 1$.

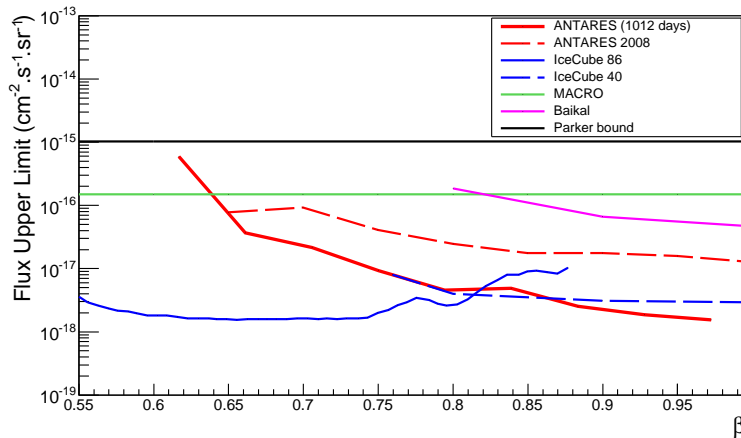


Figure 5: ANTARES 90% C.L. upper limit on flux for MMs using five years of data with 1012 active days live time (solid red line), compared to the upper limits obtained by other experiments [9, 7, 8], as well as the previous analysis of ANTARES (dashed red line) [11] and the theoretical Parker bound [5]. In [9] a more optimistic model for δ -rays production of MMs is used, making a direct comparison difficult.

The limits presented show a good result at high velocities. Below the Cherenkov threshold $\beta = 0.74$, the model of cross section for interactions between monopoles and electrons used in this analysis is the Mott model [15], which provides less light compared to the KYG model [14] used by IceCube, making a direct comparison between the two results difficult. The use of the Mott cross section allows a simpler application in time-consuming Monte Carlo simulations of the energy spectrum of the produced δ -electrons. Additionally, the Mott prediction yields a safer and conservative estimate of the total light yield.

This analysis opens a new window to the search for magnetic monopoles using the future detector KM3NeT [24] that will certainly improve the sensitivity to their detection due to its large volume and high detection performance.

References

- [1] P.A.M. Dirac, *Proc. R. Soc. A* **133** (1931) 60.
- [2] G. 't Hooft, *Nucl. Phys. B* **79** (1974) 276.
- [3] A.M. Polyakov, *Sov. Phys. JETP Lett.* **20** (1974) 194.
- [4] A.H. Guth, *Phys. Rev. D* **23** (1981) 347.
- [5] E.N. Parker, *Astrophys. J* **160** (1970) 383.
- [6] B. Acharya et al., *JHEP* **08** (2016) 067.
- [7] M. Ambrosio et al., *Eur. Phys. J. C* **25** (2002) 511.
- [8] V. Aynutdinov et al., *Astropart. Phys.* **29** (2008) 366.
- [9] M.G. Aartsen et al., *EPJ C* **76** (2016) 133.
- [10] A. Aab et al., *Phys.Rev.* **D94** (2016) 082002.
- [11] S. Adrian-Martinez et al., *Astropart. Phys.* **35** (2012) 634.
- [12] M. Ageron et al., *Nucl. Instr. and Meth. A* **656** (2011) 11.
- [13] S.P. Ahlen, *Phys. Rev. D* **17**, 1 (1978) 229.
- [14] Y. Kazama et al., *Phys. Rev. D* **15** (1977) 2287.
- [15] S.P. Ahlen, *Phys. Rev. D* **14** (1976) 2935.
- [16] G. Carminati et al., *Comput. Phys. Commun.* **179(12)** (2008) 915.
- [17] A. Margiotta, *NIM A* **725** (2013) 98.
- [18] G.D. Barr et al., *Phys. Rev. D* **74** (2006) 094009.
- [19] L. Fusco and A. Margiotta, *EPJ Web of Conferences* **116** (2016) 02002.
- [20] J.A. Aguilar et al., *Astropart. Phys.* **34** (2011) 652.
- [21] J.A. Aguilar et al., *Astropart. Phys.* **34** (2010) 179.
- [22] G.J. Feldman and R.D. Cousins, *Phys. Rev. D* **57** (1998) 3873.
- [23] G.C. Hill and K. Rawlins, *Astropart. Phys.* **19** (2003) 393.
- [24] S. Adrian-Martinez et al., *J. Phys.* **G43(8)** (2016) 084001.

Sensitivity of the ANTARES neutrino telescope to atmospheric neutrino oscillation parameters

I. Salvadori*

Aix Marseille Univ, CNRS/IN2P3, CPPM, Marseille, France

E-mail: salvadori@cppm.in2p3.fr

On behalf of the ANTARES Collaboration

A new analysis, aimed at improving the current ANTARES measurement of the atmospheric neutrino oscillation parameters, is presented in these proceedings. Two different track reconstruction procedures are combined in order to increase the sensitivity. Furthermore, a novel method to estimate the neutrino energy is applied. A complete 3-flavour description of the oscillation probability including matter effects in the Earth is used. By performing a two-dimensional fit of the event rate as a function of reconstructed energy and zenith angle, expectations on the sensitivity to the oscillation parameters are derived. Using the same analysis chain, a study on the ANTARES sensitivity to sterile neutrinos is performed.

*35th International Cosmic Ray Conference - ICRC2017-
10-20 July, 2017
Bexco, Busan, Korea*

*Speaker.

1. Introduction

The ANTARES neutrino telescope [1] is situated in the Mediterranean Sea, 40 km from the coast of Toulon (France). It is composed of 12 detection lines, each one equipped with 25 floors of 3 optical modules (OMs), with a vertical spacing of 14.5 m. The horizontal spacing among the lines is around 60 m. The main goal of ANTARES is the observation of high energy neutrinos from galactic and extra-galactic sources. The detector is, for this reason, optimized to detect neutrinos of energies up to TeV, by detecting the Cherenkov photons emitted by charged particles produced in neutrino interactions. On the other hand, at neutrino energies of the order of GeV, the detector configuration and the reconstruction algorithms allow to study the phenomenon of atmospheric ν_μ disappearance due to neutrino oscillations, and constraints on atmospheric neutrino oscillation parameters can be derived.

The document is organized as follows: in Section 2 the mechanism of neutrino oscillations is recalled; in Section 3 the MC simulations are described; the track and energy reconstruction procedures are explained in Section 4, together with the details of the event selection; a discussion of the minimization procedure is described in Section 5 and the ANTARES sensitivity for the Δm_{32}^2 and θ_{23} parameters are presented in Section 6. In Section 7 the parameter space which can be tested under the assumption of the existence of a sterile neutrino is obtained. Conclusions and prospects are given in Section 8.

2. Neutrino Oscillations

Neutrino oscillation is a quantum mechanical phenomenon, which occurs since the neutrino mass eigenstates (ν_1, ν_2, ν_3), which are used to describe neutrino propagation through space, are not the same as the neutrino flavour eigenstates (ν_e, ν_μ, ν_τ), which are the ones taking part in interactions. The relation between these two bases is described by the Pontecorvo-Maki-Nakagawa-Sakata (PMNS) matrix [2], and can be parameterized by three mixing angles ($\theta_{12}, \theta_{23}, \theta_{13}$) and a CP violating phase (δ_{CP}).

The survival probability of atmospheric ν_μ in the 3 flavour scenario can be written as:

$$P_{\nu_\mu \rightarrow \nu_\mu} = 1 - 4|U_{\mu 1}|^2|U_{\mu 2}|^2 \sin^2\left(\frac{1.27\Delta m_{12}^2 L}{E}\right) - 4|U_{\mu 1}|^2|U_{\mu 3}|^2 \sin^2\left(\frac{1.27\Delta m_{31}^2 L}{E}\right) - 4|U_{\mu 2}|^2|U_{\mu 3}|^2 \sin^2\left(\frac{1.27\Delta m_{32}^2 L}{E}\right)$$

where L is the distance traveled by the neutrino (in km), E is its energy (in GeV), $U_{\alpha i}$ are the elements of the PMNS matrix, and $\Delta m_{ij}^2 = |m_i^2 - m_j^2|$ (in eV^2) is the absolute difference of the squares of the mass eigenstates.

In this work, a complete 3 flavour framework is used, and the survival probabilities of atmospheric muon neutrinos including Earth matter effects are computed numerically using the open source software *OscProb* [3].

3. Monte Carlo Simulations

The official Monte Carlo (MC) production of ANTARES has been used for this work, which simulates individual data acquisition "runs" from 2007 to 2015. A total lifetime of around 2236

days has been considered. Neutrino events are generated using the *GENHEN* [4] software, developed in the ANTARES Collaboration, and they are weighted with the Honda atmospheric neutrino flux [5], if not otherwise specified. For the simulation of atmospheric muon bundles, instead, the *MUPAGE* [6] software is used. Atmospheric muons wrongly reconstructed as up-going represent the main background source for this study. This program uses parametric formulas to describe the energy, zenith and multiplicity distributions of muons arriving at the detector [7].

4. Event Reconstruction and Selection

Two different track reconstruction algorithms have been combined in the analysis, in order to increase the sensitivity. A detailed description of the procedures can be found in [9] and [10], respectively.

Starting from the reconstructed muon direction, a hit selection based on spatial and time distributions is made, in order to select direct Cherenkov photons coming from the muon track. The photons are then projected back to the track to find the first and last emission point, which are then used for the muon track length estimation. Taking into account the ionisation energy loss of 0.24 GeV/m for minimum ionising muons in sea water, the muon energy is computed.

In order to reduce the contamination due to atmospheric muons, only events reconstructed as upward-going are considered in the analysis. Requiring a containment condition, based on the position of the reconstructed interaction vertex, and applying additional cuts based on quality parameters specific for each reconstruction procedure, the remaining background decreases to about 0.03 muons per day. Additional sources of background are due to neutral-current events, but these are negligible. The atmospheric neutrino signal is expected to be of around 3 neutrinos per day.

5. Minimization Procedure

MC events have been binned in a 2-dimensional histogram with 100 logarithmic bins in reconstructed muon energy, from 0.1 to 200 GeV, and 21 bins in reconstructed cosine of the zenith angle, from -1 to 0.2. A pseudo-data sample, i.e. a number of events with the same characteristic of a real data sample collected in the detector lifetime of 2236 days, has been created using MC simulations assuming the values of atmospheric oscillation parameters $\Delta m_{32}^2 = 2.43 \times 10^{-3} \text{ eV}^2$ and $\theta_{23} = 41.5^\circ$. We chose such a value of θ_{23} because is close to the current global best fit value for this parameter [11]. The expected sensitivity of the analysis to the oscillation parameters has then been tested by computing the χ^2 for each different hypothesis with respect to the test point.

The Earth density profile has been parameterized using the *PREM* model [12]. The *ROOT* class *Minuit2Minimizer* has been used to perform the χ^2 minimization in order to find the values of the atmospheric neutrino oscillation parameters which fit best our pseudo-data sample. A normal neutrino mass ordering is assumed.

The minimization procedure depends on multiple parameters which affect the oscillation pattern in zenith and energy, apart from the oscillation parameters themselves. So far, only a global normalization factor, N , is left free to account for these systematic effects. Also θ_{13} has been fitted, but with a prior. In Table 1 a complete list of all the fitted parameters together with their test values and eventual prior is presented.

Parameter	Test Point Value	Prior
N	1.00	FREE
Δm_{32}^2 [10^{-3} eV 2]	2.43	FREE
θ_{23} [$^\circ$]	41.50	FREE
θ_{13} [$^\circ$]	8.41	8.41 ± 0.28
θ_{12} [$^\circ$]	33.46	FIXED
Δm_{21}^2 [10^{-5} eV 2]	7.53	FIXED
δ_{CP} [$^\circ$]	0.00	FIXED

Table 1: Oscillation parameters (first column), values used to construct the pseudo-data sample (second column) and eventual prior (third column).

6. ANTARES Sensitivity to the Atmospheric Neutrino Oscillation Parameters

The sensitivity region is presented in form of confidence intervals in the parameter space $\theta_{23} - \Delta m_{32}^2$, which have been computed by looping on a fine grid of values around the minimum, and using tabulated critical values for χ^2 with 2 degrees of freedom (dof). In Figure 1 the sensitivity at 90% C.L. obtained from the analysis of the pseudo-data sample used is compared with the results from other experiments. The one-dimensional contours are also shown. They have been obtained by looping over the same grid of values of Δm_{32}^2 and θ_{23} , respectively, and minimizing with respect to the other free parameters of the fit.

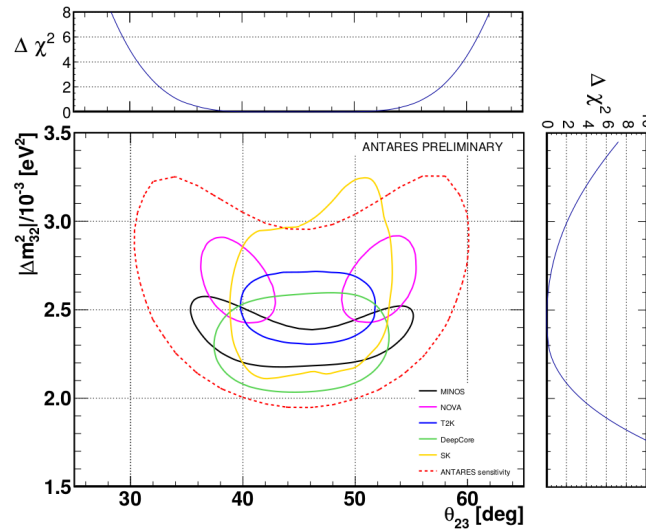


Figure 1: Result obtained from our pseudo-experiment simulating 2236 days of ANTARES lifetime. The red-dashed curve represents the allowed parameter region at 90% C.L. The one-dimensional contours for the two oscillation parameters under study are also shown. For comparison, results from MINOS [13], NOvA [14], T2K [15], IceCube (DeepCore) [16] and Super Kamiokande [17] are also shown.

7. ANTARES Expected Sensitivity to Sterile Neutrinos

The existence of additional neutrinos, which do not take part in the weak interaction but whose

presence could introduce distortions in the oscillation probability patterns, has been posited as a possible explanation for some neutrino experiment anomalies [18]. Here, only the simplest 3 + 1 model is considered, which describes the mixing between the three active neutrinos with only one sterile neutrino.

Figure 2 illustrates the effect that the existence of such a sterile neutrino would have on the oscillation probability of a vertically up going muon neutrino crossing the Earth, as a function of its energy.

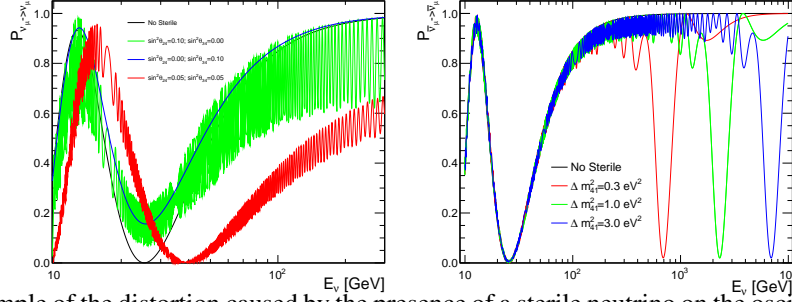


Figure 2: Example of the distortion caused by the presence of a sterile neutrino on the oscillation probability pattern, for a vertical up going ν_μ (left panel) and $\bar{\nu}_\mu$ (right panel), as a function of the neutrino energy.

As shown in the figure, two different energy ranges can be studied. The first one, around 20 – 30 GeV is sensitive to the mixing angles θ_{24} and θ_{34} , while the second one, around 10^3 GeV, allows to constrain the mass splitting Δm_{41}^2 .

Two parallel analyses, described in 7.1 and 7.2 respectively, have been made, in order to study the sensitivity of ANTARES to the sterile neutrino parameters. Data have been imitated with MC assuming no sterile; the standard oscillation parameters have been kept fixed to the same values as illustrated in Table 1, and a global normalization factor, N , has been left free to account for systematic effects. The details are presented in the following sub sections.

7.1 Low Energy Analysis

For the lowest energy range, the same events from the considered pseudo-data sample as for the standard oscillation analysis are used. Events have been binned in a 2D histogram with 10 logarithmic bins in reconstructed energy, from $10^{0.8}$ GeV to 10^2 GeV and 8 bins in reconstructed $\cos \theta$, from -1 to 0 .

In Table 2 a complete list of all the fitted parameters together with their test values and eventual prior is presented.

Parameter	Test Point Value	Prior
N	1.00	FREE
θ_{24} [°]	0.00	FREE
θ_{34} [°]	0.00	FREE
θ_{14} [°]	0.00	FIXED
Δm_{41}^2 [eV ²]	N/A	FIXED at 0.5

Table 2: Oscillation parameters (first column), values used to construct the pseudo-data sample (second column) and eventual prior (third column).

A χ^2 test has been performed and sensitivity confidence intervals on the reduced parameter space $\sin^2 \theta_{24} - \sin^2 \theta_{34}$ have been built, by looping over a fine grid of values around the minimum, and using tabulated critical values for χ^2 with 2 dof. Results are shown in Figure 3.

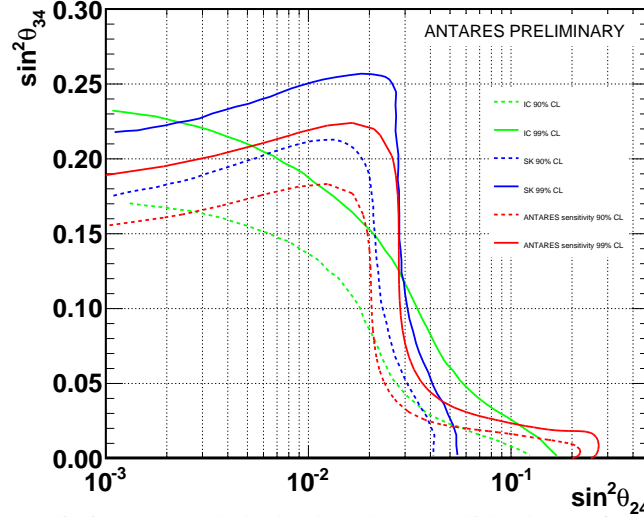


Figure 3: Expected upper limits at 90% (dashed red) and 99% (solid red) C.L. for the analysis of our pseudo-data sample. Exclusion regions are on the right side of the lines. For comparison limits from IceCube [19], and from Super Kamiokande [20] are also shown.

It is worth to remind that the standard oscillation parameters have been kept fixed for the moment. These parameters are expected to induce the largest uncertainties in this analysis. The next step in this study will be the inclusion of the neutrino mixing parameters, Δm_{32}^2 and θ_{23} , as free parameters in the fit.

7.2 High Energy Analysis

For the analysis at higher energies, events reconstructed by a dedicated track reconstruction algorithm, specific for more energetic events, have been considered. The Bartol model for the atmospheric neutrino flux [21] has been used to weight these events. A 2D fit in 10 logarithmic bins from 100 GeV to 10 TeV and 21 bins from -1 to 0.24 in $\cos \theta$ has been performed.

In Table 3 a complete list of all the fitted parameters together with their test values and eventual prior is presented.

Parameter	Test Point Value	Prior
N	1.00	FREE
θ_{24} [°]	0.00	FREE
θ_{34} [°]	0.00	FIXED
θ_{14} [°]	0.00	FIXED
Δm_{41}^2 [eV ²]	N/A	FREE

Table 3: Oscillation parameters (first column), values used to construct the pseudo-data sample (second column) and eventual prior (third column).

A χ^2 test has been performed and sensitivity confidence intervals on the reduced parameter space $\sin^2(2\theta_{24}) - \Delta m_{41}^2$ have been built, by looping over a fine grid of values around the minimum. Results are shown in Figure 4.

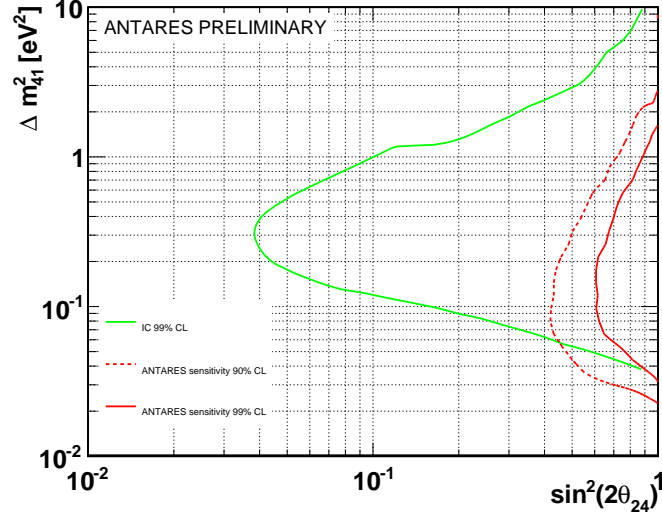


Figure 4: Expected upper limits at 90% (dashed red) and 99% (solid red) C.L. for the analysis of our pseudo-data sample. Exclusion regions are on the right side of the lines. For comparison the 99% C.L. from IceCube [22] is also shown.

It can be seen that the sensitivity regions obtained by the study of our pseudo-data sample are slightly shifted toward lower values of Δm_{41}^2 with respect to the limits presented by the IceCube Collaboration [22]. This can be explained considering the fact that the true energy distribution of our selected events is peaked at lower energy.

8. Conclusions and Outlook

A study on the sensitivity of the ANTARES neutrino telescope to the standard atmospheric neutrino oscillation parameters has been performed. A parallel study on the sensitivity to sterile neutrino parameters, in two different energy ranges, has been conducted.

Further improvements of the analysis before the *unblinding* of real data sets will include the treatment of different sources of systematic effects, in order to study their impact on the final result and a refinement of the quality cuts for selecting events.

References

- [1] ANTARES Collaboration, *ANTARES: the first undersea neutrino telescope*, *Nucl.Instrum.Meth.* A656 11-38 (2011).
- [2] C. Patrignani et al., *Particle Data Group*, *Chin. Phys. C*, **40** 100001 (2016).
- [3] <https://github.com/joaoabcoelho/OscProb>
- [4] ANTARES Collaboration, *The Run-by-Run Monte Carlo simulation for the ANTARES experiment*, in proceeding of *Very Large Volume Neutrino Telescope (VLVnT-2015)* **116** 02002 (2016).

- [5] <http://www.icrr.u-tokyo.ac.jp/mhonda/nflx2014/index.html>
- [6] G. Carminati et al., *Atmospheric MUons from PArametric formulas: a fast GEnerator for neutrino telescopes (MUPAGE)*, *Comput. Phys. Commun.* **179**, (915-923), (2008).
- [7] Y. Becherini et al., *A Parameterisation of single and multiple muons in the deep water or ice*, *Astropart. Phys.* **25** 1-13 (2006).
- [8] <http://antares.in2p3.fr>.
- [9] ANTARES Collaboration, *A Fast Algorithm for Muon Track Reconstruction and its Application to the ANTARES Neutrino Telescope*, *Astropart. Phys.* **34** (652-662) [astro-ph.IM/1105.4116v1].
- [10] E. Visser, *Neutrinos from the Milky Way*, *PhD Thesis*, Nikhef (2015).
- [11] F. Capozzi et al., *Neutrino masses and mixings: Status of known and unknown 3ν parameters*, for *Invited contribution prepared for the Nuclear Physics B Special Issue on Neutrino Oscillations celebrating the Nobel Prize in Physics 2015*, hep-ph/1601.07777v1.
- [12] A. M. Dziewonski, D. L. Anderson, *Preliminary reference Earth model*, *Physics of the Earth and Planetary Interiors* **25** (4) 297-356 (1981).
- [13] MINOS Collaboration, *Combined Analysis of ν_μ Disappearance and $\nu_\mu \rightarrow \nu_e$ Appearance in MINOS Using Accelerator and Atmospheric Neutrinos*, *Phys. Rev. Lett.* **112**, 191801 (2014).
- [14] NOvA Collaboration, *Measurement of the neutrino mixing angle θ_{23} in NOvA*, *Phys. Rev. Lett.* **118**, 151802 (2017) [hep-ex/1701.05891].
- [15] T2K Collaboration, *Measurements of neutrino oscillation in appearance and disappearance channels by the T2K experiment with 6.6×10^{20} protons on target*, *Phys. Rev.* **D91** 072010 (2015).
- [16] A. Terliuk, at *XVII International Workshop on Neutrino Telescopes*, Venice (2017).
- [17] Super-Kamiokande Collaboration, *Recent Atmospheric Neutrino Results from Super-Kamiokande in proceeding of 7th International Conference on Interconnection between Particle Physics and Cosmology*, **1604** 345-352 (2014) [hep-ex/1310.6677].
- [18] MiniBooNE Collaboration, *A Combined $\nu_\mu \rightarrow \nu_e$ and $\bar{\nu}_\mu \rightarrow \bar{\nu}_e$ Oscillation Analysis of the MiniBooNE Excesses*, hep-ex/1207.4809v2.
- [19] IceCube Collaboration, *Search for sterile neutrino mixing using three years of IceCube DeepCore data*, hep-ex/1702.05160v1.
- [20] Super-Kamiokande Collaboration, *Limits on sterile neutrino mixing using atmospheric neutrinos in Super-Kamiokande*, *Phys. Rev.* **D91** 052019 (2015) [hep-ex/1410.2008].
- [21] G.D. Barr et al., *A three-dimensional calculation of atmospheric neutrinos*, *Phys. Rev.* **D70** 023006 (2004) [astro-ph/0403630v1].
- [22] IceCube Collaboration, *Searches for Sterile Neutrinos with the IceCube Detector*, *Phys. Rev. Lett.* **117** 071801 (2016) [hep-ex/1605.01990v2].

Pointing accuracy of the ANTARES detector: Moon shadow and surface array analysis

Matteo Sanguineti* on behalf of the ANTARES collaboration

Università degli Studi di Genova, INFN Genova

E-mail: matteo.sanguineti@ge.infn.it

The ANTARES detector is the largest neutrino telescope in operation in the North Hemisphere. One of the main goals of the ANTARES telescope is the search for point-like neutrino sources. For this reason both the pointing accuracy and the angular resolution of the detector are important and a reliable way to evaluate these performances is needed. One standard method used to verify the pointing capability of a detector and to determine the instrument resolution is to observe the Moon shadowing. This corresponds to the measurement of a deficit from a narrow solid angle region centred to the Moon position due to the absorption of primary cosmic rays and a subsequent reduced flux of secondary muons. The analysis of the ANTARES data in the interval between 2008 and 2015 shows the Moon shadow with 3.5σ significance and no evidence of a statistical significant shift from the nominal position. The results from a second, independent, study are also presented. This additional method to evaluate the pointing performance used the combined measurements of the electromagnetic component at sea level and the penetrating muons. A boat with a surface array of scintillators to detect charged particles was circled around the ANTARES telescope at various radii from its centre. The pointing performance was estimated measuring the angular correlations between the down-going showers detected by the surface array and by the muons detected underwater by the ANTARES detector. The results obtained from the two methods are consistent.

*35th International Cosmic Ray Conference — ICRC2017
10–20 July, 2017
Bexco, Busan, Korea*

*Speaker.

1. Introduction

The ANTARES neutrino telescope [1] is the largest neutrino telescope currently in operation in the North hemisphere. It is designed for the identification of possible point-like sources of high energy cosmic neutrinos.

In the point-like source studies two of the most important characteristics of the detector are the angular resolution and the absolute pointing. These parameters have been estimated with two different approaches: the “Moon shadow” and the surface array analysis.

The detector [1] is not symmetric for upward- and downward-going particles, as the detection units (the optical modules) are looking downwards at 45° in order to maximize the sensitivity for up-going neutrino-induced events. Thus, this measurement using downward-going particles represents an underestimation of the angular resolution for neutrino events.

The Moon shadow measurement is based on the research of an atmospheric muon deficit in the region around the Moon. In fact our satellite absorbs primary cosmic rays reducing the number of secondary muons produced in the atmosphere. This measurement has been performed by several collaboration: CYGNUS [2], TIBET [3], CASA [4], MACRO [5], SOUDAN [6], ARGO [7] and also IceCube [8], the other neutrino telescope currently operating at the South Pole. The results of Moon shadow analysis using the ANTARES 2008-2015 data sample are presented in Section 2.

The other approach used to estimate the pointing performance of the detector is based on the search of correlations between the down-going shower measured by a surface array of charged particle detectors located on a boat close to our neutrino telescope and ANTARES itself. Two sea campaign were performed between 2011 and 2012, the results are presented in Section 3.

2. The Moon shadow analysis

In this analysis atmospheric muons are used to estimate the pointing performance of the detector, while in the other ANTARES studies they represent the major background source. The primary cosmic protons are absorbed by the Moon disk, so a “shadow” of atmospheric muons should be visible (above 1 TeV the direction of the muons is almost collinear with the primary cosmic-ray particles). Therefore measuring the event density of down-going muon tracks, the Moon is used as a “calibration source” to verify the pointing of the detector. The data are used also to estimate the angular resolution on the measurement of downward-going atmospheric muons.

The Moon shadow deficit is measured counting the number of muons detected in 25 concentric rings with increasing radius (from 0° to 10° with steps of 0.4°) centred on the instantaneous Moon position.

A Monte Carlo simulation has been developed with the MUPAGE code [9] in order to optimize the selection criteria of the analysis. The simulation includes also the propagation of the muons in the instrumented volume, the induced emission of Cherenkov light, the propagation of the light up to the PMTs and the detector response. The Monte Carlo takes in account also the optical background caused by bioluminescence and ^{40}K decay.

The atmospheric muon tracks, both in the simulation and in the data sample, have been reconstructed with a robust track fitting procedure based on a maximisation likelihood method [10]. The two parameters that are used in the analysis optimization are the quality of the reconstructed track

Λ and the angular error of the reconstructed direction β . See further information on these variables in [11].

The Moon shadow effect is simulated rejecting the muons generated within the Moon disk, having a radius $R_{Moon} = 0.26^\circ$. Two different Monte Carlo simulation sets were generated: one considering the shadowing effect of the Moon, rejecting the muons generated within the Moon disk, and the other without this effect.

The selection criteria optimization is performed thanks to the test statistic function t

$$t = \sum_{rings} \frac{(n_m - n_{exp,NM})^2}{n_{exp,NM}} - \frac{(n_m - n_{exp,M})^2}{n_{exp,M}}, \quad (2.1)$$

where the sum is over all the rings around the Moon centre; n_m is the number of events detected in a ring, $n_{exp,M}$ is the expected number of events in “Moon shadow” hypothesis and $n_{exp,NM}$ is the expected number of events in “no Moon shadow” hypothesis.

Pseudo-experiments are generated using the two Monte Carlo simulations mentioned above in order to derive the distribution of the variable t in the hypothesis that our experimental apparatus can observe the Moon shadow or not. The test statistic allow to find cuts on quality parameters Λ and β yielding the best event selection for this analysis: track quality estimator $\Lambda > -5.9$ and angular error $\beta < 0.8^\circ$. The distribution of the test statistics obtained with the mentioned values for the quality parameter cuts and the two alternative hypotheses are presented in Fig. 1.

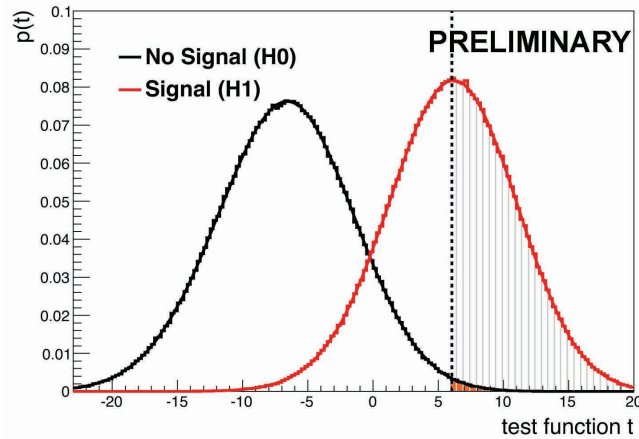


Figure 1: The test function t distribution for “Moon shadow” hypothesis (red curve) and “no Moon shadow” hypothesis (black curve). The orange area quantifies the probability that the Moon shadow effect is not observed if it actually occurs (3.4σ). The shaded area is the fraction of the toy experiments where the Moon shadow hypothesis is correctly identified as evidence of the shadowing effect (50%).

The events in the 2008-2015 ANTARES data sample have been selected with the optimized cut described above and the muon density close to the Moon region is derived. Events are binned using concentric rings around the Moon centre up to an angular distance of 10° (bin size of 0.4°). The muon density is presented in Fig. 2 .

The muon shadowing is clear close to the nominal Moon region. The angular resolution of the detector is evaluated by fitting the distribution in Fig. 2 with the following function [6]

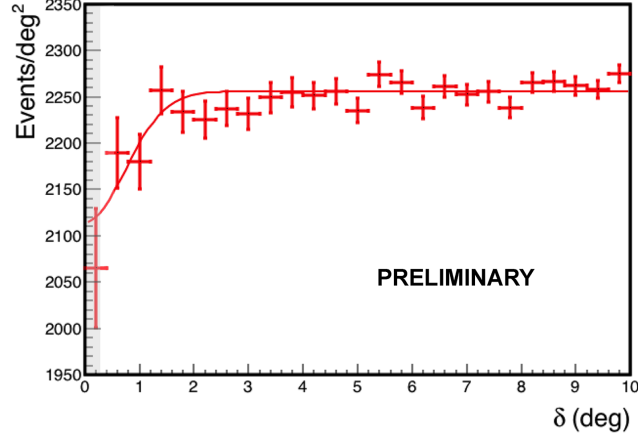


Figure 2: The muon events density as a function of the angular distance from the Moon centre. The shaded area corresponds to the apparent radius of the Moon (0.26°).

$$\frac{dn}{d\delta^2} = k \left(1 - \frac{R_{Moon}^2}{2\sigma^2} e^{-\frac{\delta^2}{2\sigma^2}} \right) \quad (2.2)$$

where k is the average muon event density in the “no Moon shadow” scenario, σ is the detector angular resolution for atmospheric down-going muons, R_{Moon} is the Moon radius (0.26°) and δ is the angular distance of the muons events from the Moon.

The measure of the angular resolution for down-going atmospheric muons resulting from the fit is $0.73^\circ \pm 0.15^\circ$. The significance of the shadowing has been evaluated using a χ^2 test on the data of Fig. 2 assuming the “no Moon shadow” scenario as null hypothesis. The corresponding significance of Moon shadowing is 3.5σ .

The absolute pointing of the detector has been evaluated with a method inspired by the approach used in [5]. A $10^\circ \times 10^\circ$ grid of square bins (bin width= 0.2°) with the centre of the grid coincident with the Moon nominal position has been considered and a test statistic function $\Delta\chi^2$ has been defined

$$\Delta\chi^2(x_s, y_s) = \chi_M^2(x_s, y_s, S_M) - \chi_{NM}^2(0) \quad (2.3)$$

where χ_{NM}^2 is the χ^2 value assuming no shadowing effect, χ_M^2 is the χ^2 value assuming that the shadowing occurs, (x_s, y_s) is the value of the assumed pointing shift and S_M is the shadowing effect strength. In the case of no shadowing the strength S_M is equal to 0.

The map of $\Delta\chi^2$ for different assumed pointing shift is presented in Fig. 3. The corresponding evaluation of confidence level of the Moon shadow pointing accuracy is shown in Fig. 4. The nominal position of the Moon (0,0) is compatible with a null shift at 1.3σ .

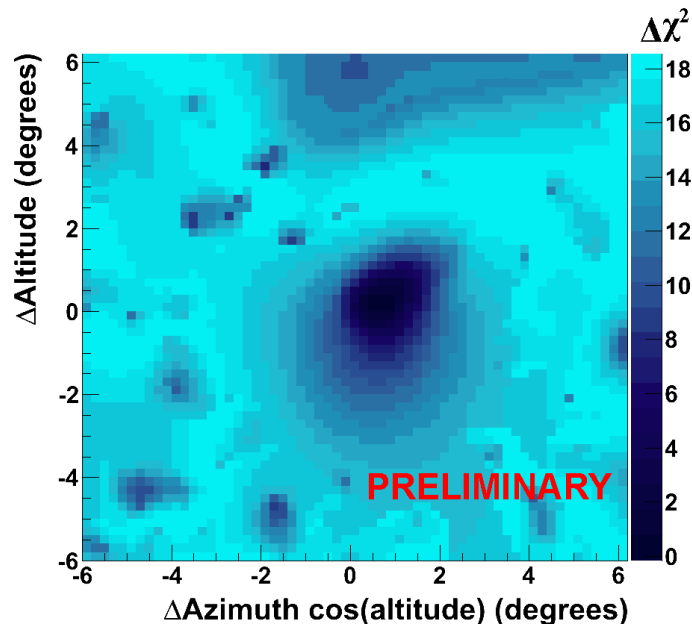


Figure 3: Map of $\Delta\chi^2$ as a function of the assumed pointing shift.

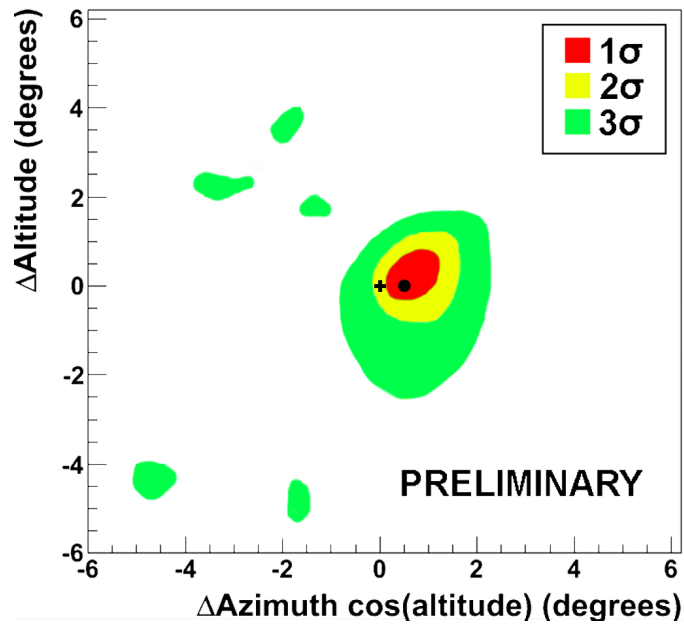


Figure 4: Contour plot of the Moon shadow pointing accuracy (red: 68% contour; yellow: 95% contour; green: 99% contour). The black dot represents the position of the most probable pointing shift.

3. Surface array analysis

Two sea campaign have been performed by the ANTARES collaboration in 2011 and 2012 where 15 liquid scintillator detection units have been located on a boat circulating around the site of the ANTARES detector. This approach allows to estimate the detector pointing performance using the coincidences between the scintillators and the telescope below.

The direction of the coincidence events was reconstructed using the known position of the boat (thanks to a GPS system) and the detector. The selection requirement for the events detected by the surface array is a coincidence in at least 3 detection units in a time window of 650 ns. This selection leads to a trigger rate of 1 Hz. On the other hand the selection criteria of the ANTARES reconstructed events in the corresponding time window are $\Lambda > -6$ and $\beta > 0.6^\circ$ (rate around 0.25 Hz).

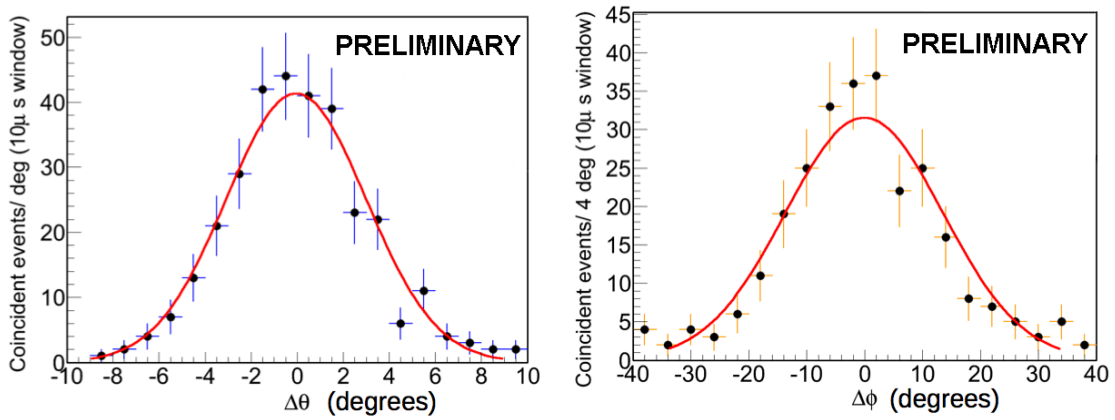


Figure 5: Difference between the shower angle evaluated with ANTARES reconstruction and the shower angle evaluated with the surface array system (using the relative position of the boat and ANTARES). Difference for zenith angle θ (left) and azimuth angle ϕ (right).

The results obtained in the two campaigns are presented in Fig. 5: The distribution of the difference between the shower angle evaluated with ANTARES reconstruction and the shower angle evaluated with the surface array system (using the relative position of the boat and ANTARES) allows to estimate the pointing performance of the detector. The surface array analysis is consistent with a correct alignment of the detector. This result is compatible with constraints derived with the Moon shadow analysis.

4. Conclusions

The absolute pointing of the ANTARES detector have been estimated exploiting the Moon shadow effect and a surface array system. The measurement has allowed also the estimation of the detector angular resolution for the measurement of atmospheric muons.

The 2007-2015 ANTARES data sample shows a 3.5σ evidence of Moon shadow effect and corresponding estimation of the detector angular resolution for atmospheric down-going muons is $0.73^\circ \pm 0.15^\circ$. The ANTARES pointing accuracy does not present any evident pointing shifts.

The Moon shadow results have been also confirmed by the surface array campaign performed between 2011 and 2012. The surface array analysis is consistent with a correct alignment of the detector.

References

- [1] M. Ageron et al. (ANTARES Coll.), Nuclear Instruments & Methods in Physics Research A656, 11-38 (2011)
- [2] D. E. Alexandreas et al., Phy. Rev., D43:1735-1738 (1991)
- [3] M. Amenomori et al., Phys. Rev., D47:2675-2681 (1993).
- [4] A. Borione et al. , Phys. Rev., D49:1171-1177 (1994).
- [5] M. Ambrosio et al., Phys. Rev., D59:012003 (1999).
- [6] H. Cobbs et al. , Phys. Rev., D61:092002 (2000).
- [7] ARGO-YBJ Collaboration, Phys. Rev., D.84:022003 (2011).
- [8] ICECUBE collaboration, Phys. Rev. D 89, 102004 (2014).
- [9] G. Carminati, A. Margiotta, M. Spurio Comput. Phys. Commun. 179, 915-923 (2008)
- [10] S. Adrian-Martinez et al. (ANTARES Coll.), JCAP 1303, 006 (2013)
- [11] A. Albert et al. (ANTARES Coll.), arXiv:1706.01857 (2017)

Monitoring of the ANTARES optical module efficiencies using ^{40}K decays in sea water

I. Salvadori* and V. Kulikovskiy

Aix Marseille Univ, CNRS/IN2P3, CPPM, Marseille, France

E-mail: salvadori@cppm.in2p3.fr, kulikovskiy@cppm.in2p3.fr

On behalf of the ANTARES Collaboration

Using the data collected by the ANTARES neutrino telescope from 2009 to 2016, the optical module (OM) efficiencies have been determined through the so called ^{40}K method. The results have been computed on a 6-day basis, after applying selection cuts in order to provide reliable time-dependent OM efficiencies for most of the individual OMs. The results show an impressive stability over time, as well as the benefit of the high voltage tuning (HVT), which is a dedicated procedure aimed to keep efficiencies at their best.

*35th International Cosmic Ray Conference - ICRC2017-
10-20 July, 2017
Bexco, Busan, Korea*

*Speaker.

1. Introduction

^{40}K is the most abundant radioactive isotope in sea water. Its Cherenkov light spectrum is equal to the one produced by muons detected by the ANTARES neutrino telescope [1]. It constitutes the principal source of background light. However, ^{40}K is as well an important calibration tool. In ANTARES, the optical modules (OMs) are arranged in groups of three (storey) and, if a ^{40}K decays near a storey, its Cherenkov light can be recorded by two OMs simultaneously. Such coincidences are dominated by ^{40}K , therefore the measured rates can be used to tune the overall OM efficiency in a detailed GEANT4 [5] simulation of the OM. This simulation provides valuable input for the global detector simulation.

The document is organized as follows: in Section 2 a brief description of the ANTARES neutrino telescope is given; the ^{40}K method for the computation of the OM efficiencies is described in Section 3; in Section 4 the used data set is presented; the fitting procedure together with the quality cuts applied are explained in Section 5, while the results of the analysis are presented in Section 6. In Section 7 a brief description of GEANT4 dedicated simulations for the overall OM efficiency is given. Conclusions and an outlook to the next generation of neutrino telescopes in the Mediterranean Sea are given in Section 8.

2. The ANTARES neutrino telescope

The ANTARES neutrino telescope was deployed in the Mediterranean Sea, 40 km from the coast of Toulon (France), at a depth of around 2.4 km. It was completed in 2008. The main goal of ANTARES is, at high energies, the study of energetic astrophysical objects. However, at lower energies, neutrino oscillations can be measured by analyzing distortions in the energy/angular spectrum of upward-going atmospheric neutrinos.

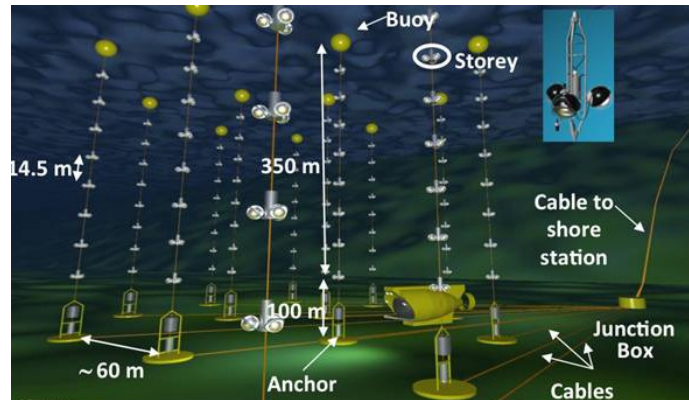


Figure 1: Schematic representation of the ANTARES neutrino telescope [2].

ANTARES is composed of 12 detection lines, each one equipped with 25 floors of 3 optical modules. Each OM holds a photomultiplier tube (PMT). The horizontal spacing among the lines is around 60 m, while the vertical spacing between the storeys is around 15 m (see Figure 1). The OMs in a storey are arranged in such a way that the axis of the PMTs points 45° downwards (see Figure 2). The photomultipliers are 10-inch tubes from Hamamatsu. The relative positions of all

OMs in the detector are monitored in real time by a dedicated positioning system.

When the distribution of the fitted charge of all PMTs in the detector shows either a broadening or a shift with respect to its nominal value, resulting in losses of efficiency and trigger bias, a dedicated procedure of high voltage tuning (HVT) is performed. The aim of this operation is to reset the effective threshold to its canonical value.

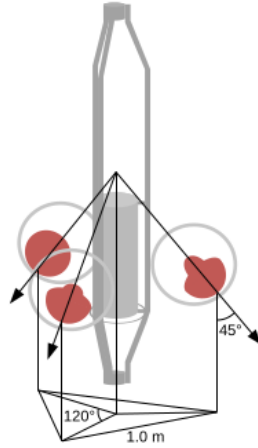
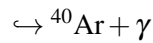
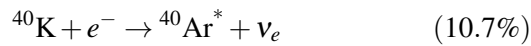
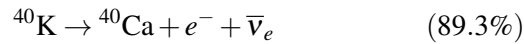


Figure 2: Schematic representation of an ANTARES storey [3]. The spheres stand for the OMs, which contain one PMT each, facing 45° downwards.

3. The ^{40}K Method

The main decay channels of ^{40}K are β decay and electron capture:



The free electron produced in the first decay channel induces Cherenkov light emission when traveling in water; fast electrons with subsequent Cherenkov light emission are also produced by Compton scattering of the photon produced by the excited Argon nuclei.

In ANTARES, if a ^{40}K decays near a storey, its Cherenkov light can be recorded by two OMs simultaneously: this is called a *genuine* coincidence. There exists also a background of *random* coincidences, which happens when two hits by two different ^{40}K decays appear to be close in time. By plotting these signals as a function of the time differences between the two OMs, the shape is that of a flat uniform background due to the random coincidences plus a Gaussian peak from the genuine coincidences. An example of such distribution is shown in Figure 3.

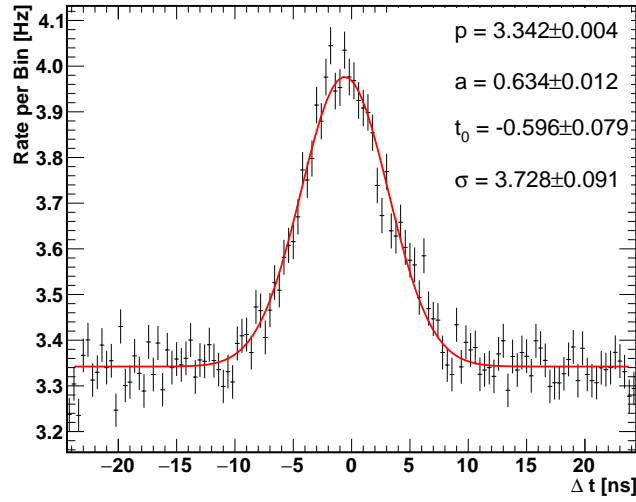


Figure 3: Example of the detected hit time differences, from ^{40}K background, between two optical modules.

The histogram of the coincidence signal is fitted with a Gaussian distribution plus a uniform one:

$$f(t) = p + a \cdot \exp\left(-\frac{(t - t_0)^2}{2\sigma^2}\right) \quad (3.1)$$

where p is the baseline, a the amplitude of the Gaussian peak due to genuine coincidences, σ is the peak width and t_0 the time offset. A mean value of $\sigma \sim 4$ ns is expected, due to the spatial distribution of the ^{40}K decays around the storey. The maximal travel distance for two photons emitted at the same place and detected by two different OMs of the same floor is the sum of the OMs distance (~ 1 m) and the photocatode diameter (~ 25 cm); considering the Cherenkov light velocity of 0.22 m/ns a time difference of 5.6 ns is expected. By averaging over the whole space a result compatible with 4 ns is found.

For perfectly calibrated OMs, t_0 would be expected at 0 ns. Deviations from the expected value of t_0 are mainly due to imperfections in time calibration. This makes the ^{40}K method also a useful tool to cross check the time calibration. However in the following we concentrate on the derivation of relative OM efficiencies from ^{40}K data.

The fit parameters can then be used to estimate the rate of events corresponding to the peak area, as:

$$R = \frac{a \cdot \sigma \cdot \sqrt{2\pi}}{T \cdot \Delta\tau} \quad (3.2)$$

where $\Delta\tau$ is the bin length used for the histogram (in this work $\Delta\tau = 0.4$ ns), and T is the total lifetime of the data set.

For each detector storey three coincidence rates are measured (R_{01} , R_{12} and R_{20}). These quantities are directly related to the sensitivities of the three OMs (s_0 , s_1 and s_2):

$$R_{ij} = R^* s_i s_j \quad (3.3)$$

where R^* is the rate for two nominal OMs with sensitivities equal to 1. In this work a value of $R^* = 15$ Hz was used. It was obtained as an average detector coincidence rate at the beginning of the analyzed data set. Solving the system of three equations the corresponding sensitivities are derived:

$$s_0 = \sqrt{\frac{1}{R^*} \frac{R_{01} R_{20}}{R_{12}}}, s_1 = \sqrt{\frac{1}{R^*} \frac{R_{12} R_{01}}{R_{20}}}, s_2 = \sqrt{\frac{1}{R^*} \frac{R_{20} R_{12}}{R_{01}}} \quad (3.4)$$

When an OM is broken, only one coincidence histogram is filled, which is not enough to determine the two efficiencies. In this case, equal sensitivities for the two working OMs are assumed, namely:

$$s_i = s_j = \sqrt{\frac{R_{ij}}{R^*}} \quad (3.5)$$

4. Data Set

Data collected from October 2009 to December 2016 have been used in this work. A dedicated ^{40}K trigger was used during the data-taking. For this trigger, coincidence hits in adjacent OMs are stored if they occur within a narrow time window of typically 50 ns. The trigger is applied with an important down-scaling factor of 200 in order not to saturate the readout chain. Taking into account this scaling factor, a total lifetime of 11 days has been analyzed. The runs have been collected in groups of 6 calendar days, which corresponds to a lifetime of around 40 minutes for each data point.

5. Procedure

The coincidence histograms are filled whenever the Δt between hits is within a maximally allowed time window, which for this work has been set to 90 ns, larger than the typical trigger time window.

All the coincidence histograms have then been fitted accordingly to Equation 3.1, from -24 ns to $+24$ ns, and some quality cuts have been applied, to ensure stable and reliable input for the subsequent efficiency calculation. The first cut on the number of entries of the histogram excludes from the analysis all those cases for which the fit fails due to lack of statistics. Taking into account the number of fitted parameters and the binning of the coincidence histograms, a χ^2 of around 116 is expected, thus, histograms with $\chi^2 > 200$ are excluded. Additional cuts on the amplitude value and its uncertainty have been applied to ensure a clear signal above background. Furthermore, expected values of the Gaussian mean and width are known, thus cuts on these parameters have been applied, in order to avoid cases in which the fit falls outside the allowed regions.

6. Results

The histograms which passed the quality cuts are then used to compute the OM efficiency, as described in Section 3. For each period analyzed, an average over all the non-zero efficiency OMs is performed. Figure 4 shows the global detector information on the OM efficiencies as a function of time.

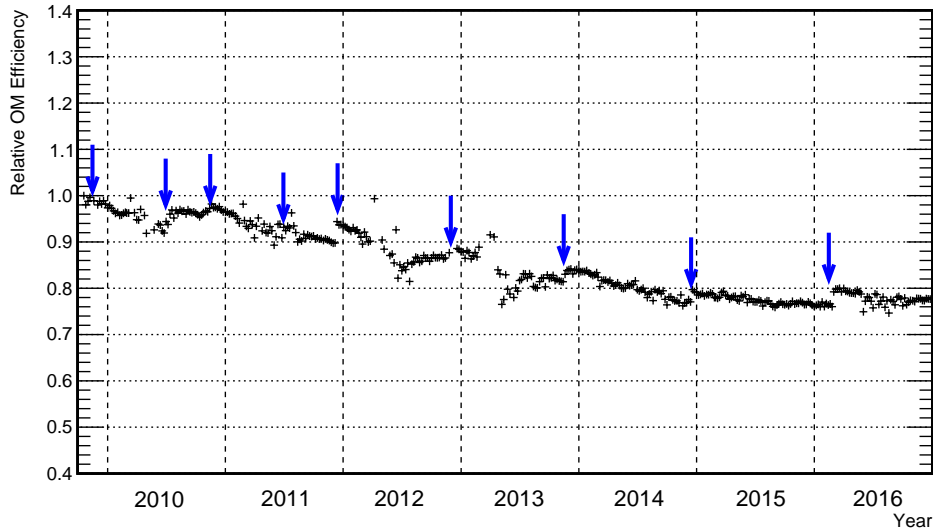


Figure 4: Relative OM efficiency over all the detector as a function of time. The blue arrows indicate the periods in which the HVT has been performed.

The values are normalized according to the first analyzed period. It can be seen that, despite the expected drop in efficiency, due to the ageing of the OMs and the consequences of biofouling, the ANTARES OMs show an impressive stability over time. An average decrease of the OM efficiency by 20%, as observed from 2009 to 2016, leads to a drop of selected atmospheric neutrino events of around 35%. However, a hypothetical astrophysical signal with a E^{-2} flux would decrease only of 15%. The effects of the HVT procedure, which is usually performed once or twice per year and allows to recover the overall efficiency periodically, can be observed as well.

7. Detailed OM calibration with simulations and ^{40}K rates

A detailed simulation is used in ANTARES to estimate the OM effective area and its dependence on the photon incident angle and wavelength [4]. These estimations are the key ingredients for the full detector simulation.

The light detection in OMs is modeled using the latest GEANT4 library [5]. A precise simulation of the photon interaction in the photocathode is performed, taking into account the optical properties of bialkali photocathodes and using a dedicated algorithm [6]. The simulation accurately reproduces the geometry of the OMs, including the glass sphere and the gel, which holds the PMT in place.

The simulation is done till the photoelectron escapes to the PMT vacuum and further signal

detection is calculated via collection efficiency, which is parameterized as a function of the photoelectron production point on the photocathode. The shape of this function is obtained by comparing PMT scans with lasers, and simulations. The absolute value of the function is tuned in order to reproduce a ^{40}K coincidence rate of 15 Hz. This is reached by setting the collection efficiency to $\sim 80\%$ at the PMT center which is physically well motivated.

8. Conclusions and Outlook

Using data collected by the ANTARES neutrino telescope with a dedicated ^{40}K trigger, the OM efficiencies have been computed until the end of 2016. The results show a good stability over time. The ^{40}K method can also be used to cross check the time calibration. The individual time dependent OM efficiencies, as calculated with the procedure presented here, are used on all recent ANTARES physics analyses.

The next generation of neutrino telescopes in the Mediterranean Sea is called KM3NeT [7]. It will be constituted by two main detectors, ARCA (Astroparticle Research with Cosmics in the Abyss), in Sicily, devoted to high energy studies, and ORCA (Oscillation Research with Cosmics in the Abyss), in France, optimised for GeV atmospheric neutrinos. The general detector layouts are similar to the one of ANTARES, with a series of detection lines, each one equipped with floors of digital optical modules (DOMs). The main difference is that each floor hosts 31 PMTs, instead of three. This allows to collect not only double coincidences from ^{40}K decays, but also multiple ones, improving the technique to compute the DOMs efficiencies as well as to study and discriminate background light.

References

- [1] ANTARES Collaboration, *ANTARES: the first undersea neutrino telescope*, *Nucl.Instrum.Meth.* A656 11-38 (2011).
- [2] <http://antares.in2p3.fr>.
- [3] ANTARES Collaboration, *Measurement of the atmospheric muon flux with a 4 GeV threshold in the ANTARES neutrino telescope*, *Astropart.Phys.*, **33**, 86-90 (2010).
- [4] C. M. F. Hugon, *GEANT4 simulation of optical modules in neutrino telescopes*, *PoS(ICRC2015)1106*.
- [5] <http://geant4.web.cern.ch/geant4/>.
- [6] D. Motta and S. Schönert, *Optical properties of bialkali photocathodes*, *NIM A*, 539 (2005) 217 - 235.
- [7] KM3NeT Collaboration, *Letter of Intent for KM3NeT 2.0*, *Journal of Physics G: Nuclear and Particle Physics*, **43** (8) 084001 (2016).